J Math Chem (2014) 52:2680–2713
DOI 10.1007/s10910-014-0411-4

ORIGINAL PAPER

Padé optimization of noise-corrupted magnetic resonance spectroscopic time signals from fibroadenoma of the breast

Dževad Belkić · Karen Belkić

Received: 22 July 2014 / Accepted: 13 September 2014 / Published online: 7 October 2014

Abstract We apply the fast Padé transform (FPT) to time signals as encoded via magnetic resonance spectroscopy (MRS) in breast fibroadenoma. Realistic levels of noise are considered. The conventional fast Fourier transform (FFT) is also used for comparison with the FPT. For $N = 2048$ signal points, the FFT generated uninformative total shape spectra with only a few distorted peaks, whereas the FPT yielded converged envelope spectra at partial signal length $N_P = 1700$. To match the FPT based at time signals sampled at $N = 2048$, the FFT requires $N = 65536$ signal points, i.e. a 32-fold lengthening of each transient. Via the parametric FPT, at $N_P = 1700$ all the resonances were resolved and metabolite concentrations precisely computed, including those that were almost completely overlapping (phosphocholine and phosphoethanolamine whose chemical shifts are separated by 0.001 parts per million). The multi-faceted signal–noise separation (SNS) procedure was applied through identification of pole-zero cancellations, zero or near zero amplitudes plus the stability test against different levels of noise. Via SNS, all the spurious resonances were confidently identified, thus leaving only genuine metabolites in the output list. Practical implications are underscored: the high resolution of the FPT will shorten the examination time of the patient. Using the FPT, the cancer biomarker phosphocholine, plus other informative metabolites can be identified and their concentrations exactly determined.

Dž. Belkić (✉) · K. Belkić
Department of Oncology-Pathology, Karolinska Institute, Building P-9, 2nd floor,
P.O. Box 260, Stockholm 17176, Sweden
e-mail: Dzevad.Belkic@ki.se

K. Belkić
School of Community and Global Health, Claremont Graduate University, Claremont,
CA, USA

K. Belkić
Institute for Prevention Research, Keck School of Medicine, University of Southern California,
Alhambra, CA, USA

Applying the fast Padé transform to time signals encoded in vivo from the breast therefore will be a key step for MRS to realize its potential to become a reliable, cost-effective method for breast cancer diagnostics.

Keywords Magnetic resonance spectroscopy · Breast cancer diagnostics · Mathematical optimization · Fast Padé transform

Abbreviations

ADC	Apparent diffusion coefficient
Ala, ALA	Alanine
β-glc, β-GLC	β-Glucose
BW	Bandwidth
CT	Computerized tomography
Cho, CHO	Choline
DFF	Denoising Froissart filter
DTI	Diffusion tensor imaging
DWI	Diffusion-weighted imaging
FFT	Fast Fourier transform
FPT	Fast Padé transform
FWHMax	Full width at half maximum
FWHMin	Full width at half minimum
GPC	Glycerophosphocholine
m-Ins, M-INS	Myoinositol
MR	Magnetic resonance
MRI	Magnetic resonance imaging
MRS	Magnetic resonance spectroscopy
MRSI	Magnetic resonance spectroscopic imaging
NMR	Nuclear magnetic resonance
PC	Phosphocholine
PCM	Personalized cancer medicine
PE	Phosphoethanolamine
PET	Positron emission tomography
ppm	Parts per million
RMS	Root-mean-square
SNR	Signal-to-noise ratio
SNS	Signal–noise separation
tau, TAU	Taurine
tCho, tCHO	Total choline
TSP	3-(trimethylsilyl-)3,3,2,2-Tetradeutero-propionic acid
ww	Wet weight

1 Introduction

Among women throughout the world, breast cancer is the most often diagnosed malignancy and one of the most frequent causes of deaths due to cancer [1–3]. The most

critical factor impacting upon survival is the stage at which breast cancer is diagnosed [4]. Screening for breast cancer has been demonstrated to significantly improve survival. This is due to early detection, such that adequate and timely care can be provided [5,6]. Intensive screening, beginning at a relatively early age has been shown to definitely benefit women at high risk for breast cancer [7]. Furthermore, women at very high risk appear to prefer intensive screening rather than other available options such as undergoing prophylactic mastectomy [8,9]. Currently, consensus is still lacking as to the best imaging strategies for early breast cancer detection, especially for women at increased risk [10]. There is consensus, however, that screening programs need to be improved and made more cost effective [3].

In this paper we will address this topic from the vantage point of mathematical optimization through advanced signal processing of relevance to magnetic resonance spectroscopy (MRS) for breast cancer diagnostics. In order to contextualize our focus and thereby help make a link to practical solutions, we will first concisely present a state-of-the-art review of the imaging modalities now in use for breast cancer screening.

1.1 Breast cancer screening via anatomic imaging

Mammography, ultrasound and magnetic resonance imaging (MRI) are the mainstays of anatomic imaging used for breast cancer screening. These are applied not only for initial breast cancer detection, but also for staging, assessment of response to therapy and post-therapeutic surveillance.

Mammography is most frequently used for breast cancer screening, notwithstanding its rather low specificity, such that false positive results occur quite often [11,12]. Deleterious consequences of these false positive findings include anxiety and uneasiness, as well as potentially deterring women from subsequently participating in breast cancer screening programs [13]. This is especially the case among women who, on the basis of mammographic findings, were sent for open surgical biopsy with a non-malignant result [14].

Mammography also entails exposure to low-energy X-radiation. It has been reported that more mutational damage may occur thereby compared to exposure to high-energy X-rays [15]. Since it is recommended that women at high risk should start screening at a relatively young age and do so relatively frequently, this radiation exposure is a serious concern. Even more worrisome is that a substantial percentage of women at high breast cancer risk are genetically susceptible to radiation-induced cancers [16,17].

The chance for false negative findings is also a concern with mammography when breast density is high. This is often the case among women at risk, especially younger women [10]. With poor sensitivity the chances of late detection obviously increase, thus impacting upon prognosis.

Ultrasound examination can be helpful in improving breast cancer detection among women with mammographically dense breasts [18,19]. However, the specificity of ultrasound is poorer than for mammography. Consequently, even more women who undergo ultrasound examination will be sent for biopsy of benign lesions [18].

Contrast-enhanced MRI is the anatomic imaging modality which generally has the best sensitivity for detecting breast cancer, especially among women at high risk

[17,20–22]. Moreover, MRI does not entail exposure to ionizing radiation. On the other hand, MRI has lower specificity than mammography. Consequently, MRI is associated with high biopsy rates, with the majority of cases being for benign lesions [6]. There are several non-malignant breast lesions that are difficult to distinguish from breast cancer on MRI. Among the benign breast pathologies that can resemble cancerous lesions on MRI are fibroadenomas, as well as benign proliferative breast disease, papillomas, desmoid tumors and inflammatory lesions [23–25]. Using dynamic contrast-enhanced MRI, non-mass morphology and small lesions of the breast are also hard to identify as benign [26,27].

By participating in intensive surveillance programs women at high breast cancer risk appear to be reassured by the excellent sensitivity of MRI [28]. However, the increased chance of false positive findings can adversely affect quality of life [10,29]. Moreover, once this occurs, women may be reluctant to continue with intensive screening using MRI. A fairly recent study [30] reports that only 58 % of women at high breast cancer risk agreed to participate in an MRI screening program to which they were invited. The chances of being sent for biopsy or other testing, as well as fear were among the reasons cited for non-participation. It should also be noted that the specificity of MRI becomes even lower after excisional biopsy [31].

False negative scans from MRI can occur with e.g. small cancerous lesions if they do not selectively take up contrast agent. Moreover, breast cancer has been reported to arise within benign lesions such as fibroadenomas [32]. The use of susceptibility-weighted three-dimensional MRI may allow the utilization of phase evolution to visualize microcalcifications [33]. Still, however, mammography, rather then MRI continues to be the method of choice for detecting and characterizing these diagnostically-important microcalcifications.

Another major problem with MRI is its high cost. As a consequence, it is only for women at very high risk of breast cancer that MRI is considered to be a cost-effective screening method [18].

Overall, anatomic imaging modalities are insufficiently specific, generating a large number of false positive findings. Functional as well as molecular imaging have much to offer in this regard [34–36]. In particular, magnetic resonance (MR)-based modalities, including diffusion-weighted MRI could be appropriate for breast cancer screening/surveillance, since, as noted, MR is free from ionizing radiation.

1.2 Diffusion-weighted MRI for breast cancer diagnostics

Non-malignant lesions can often be distinguished from cancer via diffusion-weighted imaging (DWI). The random (Brownian) motion of free water is assessed, providing insights into local tissue architecture. Since malignancy is frequently associated with increased cellularity or intracellular density, the motion of free water molecules may be restricted. This is reflected in a decreased apparent diffusion coefficient (ADC). An increased ADC is usually observed with benign lesions [37]. Important exceptions do exist however. In the breast, a low ADC is observed with fibrotic tissue or with benign proliferative changes, whereas necrosis which may occur in malignant tissue is associated with an increased ADC. The reason for this is that necrosis is hypocellular.

Non-mass breast lesions are not easily evaluated with DWI [38]. Although certain technical advances in ADC have been reported that assist in voxel positioning and measuring ADC in breast tumors [39,40], there are substantial problems in choosing the cutpoints and recording parameters for DWI. Consequently, the distinction between benign and malignant breast lesions using DWI cannot yet be made with adequate certainty [36,41].

The intrinsic diffusion properties of biological tissues can be modeled via an extension of the scalar diffusion coefficient as a second-order symmetric and positive-definite tensor **D**. Through diffusion tensor imaging (DTI) eigenvalue decomposition is performed to diagonalize the tensor to obtain three eigenvalues $(\lambda_1, \lambda_2, \lambda_3,$ where $\lambda_1 \geq \lambda_2 \geq \lambda_3)$ and three eigenvectors $(\mathbf{e}_1, \mathbf{e}_2, \mathbf{e}_3)$. These provide a complete description of the geometric and diffusion properties of the tensor [42]. Recent studies [43,44] applying DTI-derived vector and parametric maps indicate that the breast architecture can thereby be evaluated with high spatial resolution. Comparisons between twenty-six women with 33 cancerous breast lesions and fourteen women with 20 benign breast lesions revealed lower ($p < 0.0009$) orthogonal diffusion coefficients $\lambda_1, \lambda_2, \lambda_3$ in the malignant lesions, with a specificity of 98 %. More studies on larger groups of women in these two categories are expected to be forthcoming.

1.3 Breast cancer diagnostics using magnetic resonance spectroscopy or spectroscopic imaging

Molecular imaging via MRS or magnetic resonance spectroscopic imaging (MRSI) can potentially provide further distinction between breast cancer and non-malignant breast lesions. The metabolic characteristics of tissue can be elucidated by MRS, and thereby the specificity of MRI is improved for distinguishing breast cancer from benign breast lesions [45–47]. Often a single MRS voxel does not adequately represent the scanned tissue. Multi-voxels assessed via MRSI can then provide volumetric coverage, and investigations of breast cancer as well as benign breast lesions have also been reported using MRSI [48–50].

1.3.1 Assessment of total choline via MRS and MRSI

Published results using in vivo proton MRS or MRSI with 1.5T or 3T scanners have been recently compared for over 700 cancerous versus over 400 non-malignant breast lesions [51]. Most of these studies have assessed the composite or total choline (tCho) peak, with a resonant frequency at approximately 3.2 parts per million (ppm). As a reflection of cell membrane turnover, tCho is used as an indicator of cancer [47]. A meta-analysis [51] of MRS data based upon estimates of tCho from 1200 breast lesions indicates a pooled sensitivity of 73 % (556 of 761) and specificity 88 % (386 of 439). Due to publication bias, however, the authors suggest that these pooled ratings may overestimate the diagnostic accuracy of MRS [51]. In most of the studies included in the meta-analysis [51] an arbitrary cutpoint for the ratio of the tCho peak to baseline noise was used as the indicator of malignancy.

Signal-to-noise ratio (SNR) increases linearly with magnetic field strength. Thus, higher field scanners could improve SNR, and would be expected to enhance MRS-based diagnostics of the breast [45]. Smaller lesions could thereby be better evaluated, since smaller voxel size could be used [52]. Contrary to these expectations, however, the diagnostic accuracy of MRS in distinguishing benign breast lesions from breast cancer was not found to be superior in studies using 3 T scanners [53,54] compared to those using 1.5 T scanners [51]. There have been some published data using even higher field (4 or 7 T) MR scanners [52,55–59]. Whereas tCho levels were significantly elevated in breast cancer in an investigation [56] of 500 in vivo breast spectra using a 4 T scanner, tCho was also reported as being present in many benign breast lesions and in normal breast. On the other hand, tCho was undetectable in several breast cancers. Considerable overlap was observed among the ranges of tCho for these three categories of breast tissue. Although MR imaging for breast via higher field MR scanners is reportedly feasible from a technical vantage point [59,60], the enormous costs (roughly $1 million per tesla) [61], would bar high-field scanners from most breast cancer screening protocols.

Overall, tCho as a single composite spectral entity does not provide sufficient diagnostic accuracy for breast cancer screening. On the one hand, choline may be detected in fibroadenoma and other benign breast lesions as well as in normal breast, whereas especially in small tumors, on the other hand, choline may not be found. During lactation, choline generally appears in normal breast, although a lactose resonance at 3.8 ppm is also usually observed [62]. Importantly, breast cancer and lactation can coexist and the former is typically detected late [63]. Another problem is that many different cut-points for tCho have been used to define breast cancer versus benign breast. Standardization is thus very tenuous.

1.3.2 Conventional data processing in MRS and MRSI: overlapping resonances cannot be handled

Isolated resonances do indeed become sharper and better resolved when higher field scanners are employed. However, peak widths of overlapping resonances are broadened on spectra generated from MRS data acquired using stronger magnets [64]. This problem is important because overlapping resonances are very abundant in MR spectra [35], especially of the breast. Due to lipid-induced sidebands, the detection of choline can be compromised when using higher field magnets [65]. Usually these lipids are suppressed, since dominant fat of the breast also hampers localized shimming. By increasing the echo time, lipid suppression can be achieved. However, lipid may be part of the actual disease process, and thereby important diagnostic information might be lost [66]. Other potentially informative metabolites with short T_2 relaxation time will also have decayed with the use of long echo times.

In vitro nuclear magnetic resonance (NMR) applied to extracted specimens yields richer metabolic information, much of which is relevant to breast cancer [67]. Notably, tCho contains several components that can better differentiate benign from malignant breast tissue. Among these are phosphocholine (PC) resonating at approximately 3.22 ppm, glycerophosphocholine (GPC) at 3.23 ppm, as well as free choline (Cho) at 3.21ppm [68]. With malignant transformation of mammary cells, two pathways,

phosphorylation and oxidation of choline, are increased [68]. Consequently, PC is augmented whereas choline-derived ether lipids are suppressed. A "glycerophosphocholine to phosphocholine switch" occurs with malignant transformation in the breast. This is associated with over-expression of the enzyme choline kinase responsible for PC synthesis [68–70].

Increased levels of phosphocholine and elevated PC to GPC ratio are considered to be indicators of malignant transformation of the breast [70,71]. However, the resonant frequencies of PC, GPC and free choline are very close to one another. Moreover, according to NMR data from extracted breast specimens [67], the much more abundant phosphoethanolamine (PE) also resonates at ~ 3.22 ppm and thereby completely hides the PC peak at 3.22 ppm on total shape spectra.

Data analysis of conventional applications of in vivo MRS and MRSI relies upon the fast Fourier transform (FFT), built into all existing clinical MR scanners. The FFT is used to transform the encoded MRS time signal into its spectral representation in the frequency domain. However, the FFT is a non-parametric, linear method which can generate only a total shape spectrum or envelope. No information whatsoever can be gleaned about the underlying components via Fourier analysis. Consequently, the FFT cannot disentangle the overlapping resonances contained within the tCho peak. No reliable information can be obtained about the relative abundance of the components of tCho, i.e. PC, GPC, free choline, nor about the concentration of PE which, as mentioned, completely overlays PC. The number of overlapping resonances contained within a given peak cannot be ascertained via the FFT. Instead, post-processing via fitting is used to merely guess how many components underlie a given peak. Obviously, there is a great likelihood that false information will be generated by overfitting and/or that true metabolites are missed due to underfitting. Clearly, then, fitting procedures cannot provide reliable quantitative information even about any predetermined resonances, since these are most likely biased, and at best, only by serendipity yield a correct guess [72]. Simply stated, the inability to autonomously reconstruct the spectral parameters, i.e. the fundamental complex frequencies and amplitudes, completely eliminates the FFT from the list of signal processors that can on their own solve the quantification problem, which is otherwise the "raison d'être" of MRS.

1.4 The fast Padé transform: an advanced and more appropriate signal processor for MRS and MRSI

As a more advanced signal processing method, the fast Padé transform (FPT) has capabilities that are excellently suited to NMR spectroscopy in biochemistry as well as to MRS and MRSI in medicine [72–75]. In the present context, the FPT is particularly poised to solve the above-described challenges in breast cancer diagnostics using MRS and MRSI. The FPT is a high-resolution, non-linear signal processor which has parametric as well as non-parametric forms.

The actual number of metabolites contained in a given encoded MRS time signal is treated as a parameter by the FPT, and is precisely ascertained. The complex-valued fundamental frequencies and amplitudes of the characteristic oscillations of each resonance are the spectral parameters that are uniquely determined. Thereby, the key clinical information, the metabolite concentrations are reliably computed.

These features of the FPT apply even to the most closely-overlapping resonances, with quantification achieved to machine accuracy for theoretically synthesized noiseless time signals [72,74–76].

The FPT generates a spectrum by the quotient of two polynomials (P/Q). The fast Padé transform has two equivalent variants denoted by $\mathrm{FPT}^{(+)}$ and $\mathrm{FPT}^{(-)}$ as defined inside and outside the unit circle for the causal and anti-causal representation, respectively [72–75]. Both the $\mathrm{FPT}^{(+)}$ and the $\mathrm{FPT}^{(-)}$ are used for cross validation, such that only those converged results of reconstructions obtained by both the $\mathrm{FPT}^{(+)}$ and the $\mathrm{FPT}^{(-)}$ are retained. Thus, convergence must be attained via two algorithms that encompass two complementary regions of the complex frequency plane, outside and inside the circle of radius equal to 1. This is a self-contained checking procedure such that there is no need to compare it with any other signal processor to validate the results of the FPT.

The FPT has been effectively applied to many in vivo encoded MRS time signals [72,73,77–79]. Nevertheless, for benchmarking within cancer diagnostics, it is deemed necessary to apply the FPT to simulated or synthesized MRS time signals that closely correspond to the encoded data. This strategy is vital to validation because it is akin to the controlled approach used in other disciplines such as engineering, and has thereby passed "the test of time" [72,73].

1.4.1 How signal–noise separation is achieved by the fast Padé transform

Spurious resonances are abundant in most MRS quantification problems solved by the FPT, since such problems invariably generate an over-determined system of linear equations. The FPT algorithmically separates the genuine and spurious resonances by identifying pole-zero confluences. This is a phenomenon unique to the FPT. When the FPT generates a spectrum by the quotient of two polynomials (P/Q), the intrinsic characteristics of the system are parametrized. This is achieved through the unique set of spectral poles and zeros. The denominator polynomial Q is associated with the system poles and represents the positions (chemical shifts) and widths of peaks in a spectrum. The numerator polynomial P corresponds to valleys in between any two adjacent peaks in the same spectrum, and the system zeros are described thereby. The poles and zeros that are coincident are called Froissart doublets [80]. These doublets are unstable; they roam chaotically in the complex frequency plane thus exhibiting instability with even the slightest perturbation, and do not ever converge. This stochastic behavior is typical of noise. Thus, in many ways spurious resonances are similar to noise and, as a spurious content, need to be identified and binned to be cast out from the final results of the analysis.

Before the analysis, the total number K of genuine resonances is not known. Using the "FFT + fitting" approaches only a guess can be made about K. By contrast, the FPT exactly reconstructs this number K, just as it reconstructs the other spectral parameters: the fundamental frequencies and amplitudes. When the genuine resonances fully converge, the sought number K is determined.

As a single polynomial, the FFT brings over all the noise from the time domain into the frequency domain. There is consequently no way for the FFT to cancel or suppress this noise. In contradistinction, since the FPT is comprised of two polynomials P and

Q, these two degrees of freedom provide richer mathematics. The quotient P/Q in the FPT is unique and facilitates noise suppression, by the following logic. In the reconstructed spectrum $P_{K'}/Q_{K'}$, the total number of resonances K' is larger than its genuine counterpart K in the unknown ratio P_K/Q_K. The overestimation $\Delta K = K' - K$ is equally distributed between $P_{K'}$ and $Q_{K'}$. Consequently, $P_{K'}$ and $Q_{K'}$ will have an equal number of the same spurious resonances in $P_{K'}/Q_{K'}$. This excess, spurious content cancels out in $P_{K'}/Q_{K'}$. After this cancellation, only the true information P_K/Q_K remains in the reconstructed data. The number K of physical, genuine resonances is thereby exactly determined, even without quantification, as it is only necessary to extract P_K/Q_K from the time signal. The common degree of polynomials $P_{K'}$ and $Q_{K'}$ is gradually increased until convergence has been reached in their quotient $P_{K'}/Q_{K'}$ to the limit ratio P_K/Q_K. This convergence criterion removes the false information and keeps that which is genuine. A kindred occurrence is seen in experiments when measurement errors for two quantities A and B tend largely to cancel in their ratio A/B.

Another way to conceptualize pole-zero coincidence is as the cancellation between a resonance (a peak) and an anti-resonance (a dip), or between a full width at half-maximum (FWHMax) and full width at half-minimum (FHWMin). Thus, spurious resonances have: FWHMax = FHWMin, whereas the poles and zeros of genuine resonances are not equal to each other and FWHMax $\neq$ FHWMin.

Overall, pole-zero cancellation is carried out by gradually increasing the degree of the Padé polynomials. Thereby, the reconstructed spectra fluctuate until stabilization occurs. This pole-zero cancellation is best seen from the cannonical representation of e.g. the diagonal FPT$^{(-)}$:

$$\frac{P_K^-(z^{-1})}{Q_K^-(z^{-1})} = \frac{p_K^-}{q_K^-}\frac{\prod_{k=1}^{K}(z^{-1}-z_{k,P}^{-1})}{\prod_{k=1}^{K}(z^{-1}-z_{k,Q}^{-1})}, \tag{1}$$

where p_K^- and q_K^- are the expansion coefficients of the largest power z^{-K} in $P_K^-(z^{-1})$ and $Q_K^-(z^{-1})$, respectively. Further, quantities $z_{k,P}^{-1}$ and $z_{k,Q}^{-1}$ are the solutions of the characteristic equations $P_K^-(z^{-1}) = 0$ and $Q_K^-(z^{-1}) = 0$, respectively, with $1 \leq k \leq K$.

Using the quotient form of Eq. (1), the terms in the Padé numerator and denominator polynomials cancel out when the computation is continued after the stabilized value of degree K in the FPT$^{(-)}$ has been attained. Hence, this is a signature of stability of the spectra:

$$\frac{P_{K+m}^-(z^{-1})}{Q_{K+m}^-(z^{-1})} = \frac{P_K^-(z^{-1})}{Q_K^-(z^{-1})} \quad (m = 1, 2, 3, \ldots). \tag{2}$$

The Cauchy residue of P_K^-/Q_K^- from Eq. (1) represents the amplitudes d_k^-. The latter have two equivalent analytical expressions:

$$d_k^- = \frac{p_K^-}{q_K^-}\frac{\prod_{k'=1}^{K}(z_{k,Q}^{-1}-z_{k',P}^{-1})}{\prod_{k'=1,k'\neq k}^{K}(z_{k,Q}^{-1}-z_{k',Q}^{-1})} \quad \text{or} \quad d_k^- = \left\{\frac{P_K^-(z^{-1})}{(d/dz^{-1})Q_K^-(z^{-1})}\right\}_{z^{-1}=z_{k,Q}^{-1}}. \tag{3}$$

It is seen from Eq. (3) that whenever $z_{k,P}^{-1} = z_{k,Q}^{-1}$, the amplitude d_k^- of the poles from the Froissart doublets is exactly zero:

$$d_k^- = 0 \quad \text{for} \quad z_{k,P}^{-1} = z_{k,Q}^{-1}. \tag{4}$$

As noted, the algorithmic pole-zero coincidences can be viewed as cancellation between the FWHMax and FWHMin (FWHMax = FWHMin) or, equivalently, between the corresponding resonance and anti-resonance. For genuine resonances, recall that FWHMax $\neq$ FWHMin. Spurious resonances have zero amplitude, whereas the amplitudes of genuine resonances are non-zero.

A resonance stability test is also used to assess whether a given resonance is genuine versus spurious. By varying the partial signal length (i.e. by truncating the total signal length and preserving the same bandwidth), and/or the level of added noise, the stability of the spectral parameters of true resonances is contrasted to the instability of those that are spurious. In other words, the genuine resonances remain stable while the spurious structures roam around and do not converge. Thereby, stable and unstable resonances are categorized as physical (genuine) versus unphysical (spurious), respectively.

Instability is exhibited in alterations of spectral parameters with changes in K' and also with various levels of noise. The alterations occur in both $P_{K'}^-$ and $Q_{K'}^-$. Although these unstable resonances behave stochastically, they still show a strong correlation of their random fluctuations, such that in the poles $z_{k,Q}^{-1}$ and zeros $z_{k,P}^{-1}$, the equality $z_{k,Q}^{-1} = z_{k,P}^{-1}$ is maintained to a high degree of accuracy. In other words, these unstable resonances form couples which can be viewed as a type of deterministic behavior (a kind of order within the chaos). Thus, the fluctuating pole is accompanied by a fluctuating zero, such that they collapse into each other ($z_{k,Q}^{-1} = z_{k,P}^{-1}$). Pole-zero coincidence consequently leads to annihilation of unstable spectral structures. This pole-zero cancellation can be viewed as subtraction of two identical contributions of opposite signs in a superposition of a resonance (peak) and anti-resonance (dip) both built from unstable, and, thus, spurious harmonics $z_{k,Q}^{-1}$ and $z_{k,P}^{-1}$ stemming from $Q_{K'}^-\left(z^{-1}\right)$ and $P_{K'}^-\left(z^{-1}\right)$, respectively. Such a correlated behavior of $z_{k,Q}^{-1}$ and $z_{k,P}^{-1}$ is due to the fact that polynomials $Q_{K'}^-\left(z^{-1}\right)$ and $P_{K'}^-\left(z^{-1}\right)$ are themselves correlated because $P_{K'}^-$ is generated from $Q_{K'}^-$. Noise suppression or elimination within the FPT is accomplished by way of detection of pole-zero congruences, and is also called the denoising Froissart filter (DFF).

On the other hand, even if some physical structures may also have near pole-zero confluences or near zero amplitude, by their stability, such genuine resonances can always be distinguished from Froissart doublets. This binning within the output list of reconstructions can also be carried out via automatic classification using the conditional probability to statistically validate the estimated parameters, as done in the fast Padé transform within the PhD thesis of Ojo in 2010 [81]. More recently, the FPT in conjunction with SNS, or equivalently, DFF, has been used in the PhD thesis by Zhang [82]. Thus, the fast Padé transform accompanied by signal–noise separation or the denoising Froissart filter promisingly appears as a multi-

pronged strategy for distinguishing false from true content of the investigated time signals.

1.5 Applications of the FPT to noiseless MRS time signals from breast cancer, fibroadenoma and normal breast

Within the framework of breast cancer diagnostics, the first step was to apply the FPT to the relevant noise-free MRS time signals. We generated three such MRS time signals that were similar to in vitro MRS data as encoded from extracted breast specimens from normal, non-infiltrated breast, from fibroadenoma and from breast cancer [67]. In each of these three cases, there were nine resonances, which the FPT resolved and precisely quantified. Among these were the resonances in the spectrally dense region between 3.21 and 3.23 ppm where phosphocholine, PC, and phosphoethanolamine, PE, were almost completely overlapping. The input parameters for these two resonances were precisely reconstructed by the FPT at convergence [10,72,83].

Alongside these extremely closely overlapping resonances in the breast spectra, a large number of spurious resonances was also generated. Altogether, at convergence, there were 750 resonances retrieved, i.e. 741 that were spurious, in addition to the nine physical peaks. The FPT clearly demarcated these two categories in all cases, despite the fact that fewer than 2 % of the resonances were genuine.

1.6 Other applications of the fast Padé transform to MRS signals for cancer diagnostics

1.6.1 The FPT applied to noiseless MRS time signals from ovarian cancer

Although ovarian cancer has an excellent prognosis if detected early, this malignancy is usually detected in the late stages with very poor survival. Appropriate screening methods are vitally important but still lacking. In vivo MRS has been earmarked as the potential method of choice for ovarian cancer diagnosis, but thus far via conventional Fourier-based processing in vivo spectra are of poor quality, due to low resolution in this small, moving organ [84,85].

We first applied the FPT to noiseless time signals associated with MRS data for benign and cancerous ovarian cyst fluid from Ref. [86]. The spectral parameters for all twelve genuine metabolites, including those that were quite closely-lying, were accurately reconstructed by the FPT using very small fractions ($N/16 = 64$) of the time signal of full length $N = 1024$ [72,87,88], whereas the FFT produced completely uninterpretable spectra at these short signal lengths [72,87,88]. From these earlier studies [72,87,88], it was seen that the FPT dramatically improved SNR and resolution. Besides the twelve genuine metabolites reconstructed at convergence, some twenty spurious resonances were also produced. The latter were identified as such due to pole-zero confluence yielding Froissart doublets with zero amplitude and thereby cast out.

1.6.2 Applications of the FPT to noiseless time signals from prostate cancer

Worldwide, prostate cancer is among the most prevalent malignancies among men, with over 200000 deaths per year attributed to this disease. Screening and early detection of prostate cancer are still quite controversial, since the existing methods lack sufficient diagnostic accuracy [89,90]. These dilemmas could potentially be surmounted by MRS and MRSI, which have shown promise in a number of aspects of prostate cancer diagnosis and management [91–93]. Still, MR-based modalities are not yet considered to be appropriate for screening [94].

Prostate spectra contain several multiplet resonances that have been very difficult to assess and quantify. We have applied the FPT to noiseless in vitro data associated with encoding from normal glandular and stromal prostate, as well as from cancerous prostate [95]. The FPT resolved and accurately quantified all twenty-seven genuine resonances, including multiplets, as well as overlapping peaks of different metabolites. The metabolite concentrations which distinguish healthy from malignant prostate were thereby precisely computed [72,96,97]. A large number, approximately 300, spurious resonances were also generated at convergence. These Froissart doublets with zero amplitude were separated with confidence from the 27 genuine resonances.

1.6.3 The FPT applied to noise-corrupted MRS time signals from ovarian cancer

We proceeded to apply the FPT to MRS time signals associated with ovarian cancer in the presence of added noise [34,98,99]. With the addition of extraneous noise ($\sigma = 0.01156$ RMS, where RMS is the root-mean-square of the noise-free time signal, RMS $= (N^{-1}\sum_{n=0}^{N-1}|c_n|^2)^{1/2}$, convergence was achieved at $N/8 = 128 (N = 1024)$, with accurate reconstruction of the spectral parameters for all twelve genuine metabolites. Some 52 spurious resonances were also generated at convergence; these were recognized as Froissart doublets with pole-zero confluences and the associated zero-valued amplitude [98].

When higher levels of noise were added ($\sigma = 0.1156$ RMS, $\sigma = 0.1296$ RMS and $\sigma = 0.2890$ RMS), the Froissart doublet coincidence was not always exact. Moreover, some of the spurious resonances showed near zero amplitudes rather than actual zero amplitudes [34,99]. Since genuine metabolites might conceivably be present at very low concentrations, their peak amplitudes could be extremely small. How then would one be completely certain which of the resonances are spurious and which are genuine? This question becomes pivotal for proceeding with confidence from controlled input data to encoded time signals for which the number of resonances and their parameters are not known prior to spectral analysis.

The stability test was vital in this case. By varying the partial signal length and also by adding yet more noise, all the true metabolites, including those with very small amplitudes could be confidently identified by their stability. Spurious resonances were unstable with even a minimal change in partial signal length or noise level, and were binned for discarding, whereas all the stable and thus true metabolic information was kept in a denoised spectrum [34,99].

1.7 Performance of the FPT for noise-corrupted MRS time signals from breast fibroadenoma: the present study

Based upon the results described above, it is justifiable to apply the FPT to noise-corrupted time signals from the breast. Here, we choose a frequently occurring non-malignant pathology, namely fibroadenoma of the breast, which can, at times, be difficult to distinguish from breast cancer. We are particularly interested in how the FPT resolves the extremely closely-overlapping resonances between 3.21 and 3.23 ppm, where, as noted, due to overexpression of the enzyme choline kinase, elevated concentration of phosphocholine has been identified as a marker of malignant transformation [68–71]. In the present study, we examine the performance of the FPT in handling noise-corrupted MRS time signals in this controlled setting, as a key step aimed towards widespread clinical application of Padé-optimized MRS for breast cancer diagnostics.

2 Methods

2.1 The known MRS time signal: input data as encoded from fibroadenoma of the breast

The time signal of the typical quantum-mechanical form was generated according to:

$$c_n = \sum_{k=1}^{K} d_k \mathrm{e}^{in\omega_k\tau},\ \mathrm{Im}\,(\omega_k) > 0, \quad (0 \le n \le N-1). \tag{5}$$

The total signal length is represented by N. These input data are based upon encoded time signals from fibroadenoma of the breast, as per Ref. [67]. Each c_n is a sum of $K = 9$ damped complex exponentials $\exp(in\tau\omega_k)$ $(1 \le k \le 9)$ with complex amplitudes d_k. Herein, ω_k and d_k are the fundamental angular frequencies and amplitudes. Moreover, $\omega_k = 2\pi\ \nu_k$, where ν_k is the linear frequency. The real and imaginary parts of a complex number z are represented by $\mathrm{Re}(z)$ and $\mathrm{Im}(z)$, respectively. The time signals of the form (5) were quantified via the FPT$^{(-)}$, as described in Refs. [72–75].

Since ω_k is complex-valued, such that for $\mathrm{Im}(\omega_k) > 0$, as in (5), quantity c_n decreases exponentially over time $n\tau (n = 0, 1, 2, \ldots, N-1)$. Thus, $\exp(in\omega_k\tau) = \exp(-n\tau\ \lambda_k + in\tau\ \mu_k)$, where $\lambda_k = \mathrm{Im}(\omega_k)$ and $\mu_k = \mathrm{Re}(\omega_k)$. Consequently, the rhs of Eq. (5) is a linear combination of K exponentially attenuated frequency-dependent cosinusoids and sinusoids each of which is premultiplied by the constant, real intensity $|d_k|$:

$$d_k \mathrm{e}^{in\omega_k\tau} = \left(|d_k|\,\mathrm{e}^{i\varphi_k}\right)\mathrm{e}^{in\omega_k\tau} = |d_k|\left\{\mathrm{e}^{-n\lambda_k\tau}[\cos(n\mu_k\tau + \varphi_k) + i\sin(n\mu_k\tau + \varphi_k)]\right\}, \tag{6}$$

where φ_k is the phase of the complex amplitude d_k.

Herein, for conciseness, we present explicitly only the reconstructions of the FPT$^{(-)}$. It is verified that the converged findings are identical to those obtained from

the FPT$^{(+)}$ [72–75]. The diagonal ($M = K$) and paradiagonal ($M = K-1$) complex-valued spectra in the FPT$^{(-)}$ are:

$$G^-_{M,K}\left(z^{-1}\right) = \frac{P^-_M\left(z^{-1}\right)}{Q^-_K\left(z^{-1}\right)}, \quad P^-_M\left(z^{-1}\right) = \sum_{r=0}^{M} p_r z^{-r}, \quad Q^-_K\left(z^{-1}\right) = \sum_{s=0}^{K} q_s z^{-s}. \tag{7}$$

Therein, z^{-1} is the harmonic variable $z^{-1} = \mathrm{e}^{-i\omega\tau}$ and $\left\{p^-_r, q^-_s\right\}$ are the expansion coefficients. The unique Padé spectrum $G^-_{M,K}\left(z^{-1}\right)$ from Eq. (7) exists for the given (input) exact finite-rank Green's function $G^-(z^{-1})$ via:

$$G\left(z^{-1}\right) = G^-_{M,K}\left(z^{-1}\right) + \mathcal{O}(z^{-M-K-1}); \; G\left(z^{-1}\right) = \sum_{n=0}^{N-1} c_n z^{-n}. \tag{8}$$

Here, the symbol $\mathcal{O}(z^{-M-K-1})$ signifies the error which is a series in powers $z^{-m}(M+K+1 \le m \le \infty)$. Thus, the approximation $G\left(z^{-1}\right) \approx G^-_{M,K}\left(z^{-1}\right)$ in the general FPT$^{(-)}$ includes exactly $M + K$ signal points $\{c_n\}$ from the input data $G\left(z^{-1}\right) = \sum_{n=0}^{N-1} c_n z^{-n}$ with $M + K \le N - 1$.

In Ref. [67], the MRS time signals of length $N = 65536$ were recorded at a Larmor frequency (ν_L) of 600 MHz and with a static magnetic field strength $B_0 \approx 14.1$T. A bandwidth (BW) of 6 MHz was used, where the inverse of this bandwidth is the sampling time τ. We used a total signal length of $N = 2048$. The nine resonances were grouped into two frequency bands. The first was from 1.3 to 1.5 ppm and the second from 3.2 ppm to 3.3 ppm. Within the second band were seven resonances, including two which very closely overlapped at approximately 3.22 ppm: phosphocholine, PC resonance #4 and phosphoethanolamine, PE resonance #5 separated by 0.001 ppm. The amplitudes d_k were computed based upon the reported concentrations of metabolites $\mathrm{C_{met}}$ for a patient with fibroadenoma. Therefore, $|d_k| = 2\mathrm{C_{met}}/\mathrm{C_{ref}}$, where $\mathrm{C_{ref}} = 0.05$mM/g. The internal reference used in Ref. [67] was TSP (3-(trimethylsilyl-) 3,3,2,2-tetradeutero-propionic acid), a molecule which is not actually present in the tissue. Therefore, $|d_k| = \mathrm{C_{met}}/(25\mu\mathrm{M/g})$ of ww of the tissue. In Ref. [67] the T_2^* relaxation times were not reported. We consequently set the line widths (full-widths at half-maximum, FWHMax) to be from 0.0008 to 0.0009 ppm.

The peaks are assumed to be Lorentzian, consistent with the time signal as per Eq. (5). In the absorption mode we used mainly the diagonal and/or paradiagonal $\mathrm{Re}(P^{\pm}_K/Q^{\pm}_K)$(diagonal) or $\mathrm{Re}(P^{\pm}_{K-1}/Q^{\pm}_K)$ (paradiagonal) forms, since these two variants for $l = 0$ and $l = 1$ are empirically observed to be more stable compared to those with other values of l ($l = 2, 3, \ldots$) in $P^{\pm}_{K-l}/Q^{\pm}_K$.

The line widths are proportional to Im (ν_k). The smallest chemical shift difference of 0.001 ppm is only 1.11 to 1.25 times larger than the line widths of 8×10^{-4} to 9×10^{-4} ppm. The phases $\varphi_k (1 \le k \le 9)$ from complex-valued d_k were all set to zero. Thus, all the d_k's are real, $d_k = |d_k|$. The input data are displayed in Table 1.

We employed the parametric version of the diagonal FPT$^{(-)}$ to analyze the MRS time signal data from breast fibroadenoma. The coefficients $\{p^-_r, q^-_s\}$ of the polyno-

Table 1 Input spectral parameters, metabolite concentrations and assignments for breast fibroadenoma

n_k or #	Re(ν_k) (ppm)	Im(ν_k) (ppm)	$\lvert d_k \rvert$ (au)	C_k (μM/g)	M_k
1	1.332	0.0008	0.059	1.475	LAC
2	1.471	0.0008	0.004	0.100	ALA
3	3.212	0.0008	0.002	0.050	CHO
4	3.220	0.0008	0.003	0.075	PC
5	3.221	0.0009	0.019	0.475	PE
6	3.232	0.0008	0.003	0.075	GPC
7	3.251	0.0008	0.039	0.975	β-GLC
8	3.273	0.0008	0.014	0.350	TAU
9	3.281	0.0008	0.019	0.475	M-INS

These parameters and concentrations correspond to the in vitro data from time signals encoded in Ref. [67]. The number of the k^{th} resonance is n_k (or #), whereas Re(ν_k) and Im(ν_k) are the real and imaginary parts of the fundamental complex-valued linear frequency ν_k referring to the chemical shifts and linewidths, respectively. The phases $\varphi_k (1 \leq k \leq 9)$ from the complex-valued amplitudes d_k were all set to zero, such that every d_k is real, $d_k = |d_k| (1 \leq k \leq 9)$. The metabolite concentrations are denoted by C_k and the metabolite assignment is M_k (*LAC* lactate, *ALA* alanine, *CHO* choline, *PC* phosphocholine, *PE* phosphoethanolamine, *GPC* glycerophosphocholine, *β-GLC* β-glucose, *TAU* taurine, *M-INS* myoinositol). In all Tables and figures, chemical shifts are in parts per million or ppm, concentrations are in μ M/g, peak widths in ppm and peak heights are in arbitrary units, au

mials $P_K^- \left(z^{-1}\right)$ and $Q_K^- \left(z^{-1}\right)$ from Eq. (7) were computed from the defining equation of the diagonal FPT$^{(-)}$ via $G \left(z^{-1}\right) \approx P_K^- \left(z^{-1}\right) / Q_K^- \left(z^{-1}\right)$.

When the coefficients of the same powers of z^{-1} are equated, two systems of linear equations are generated: one for $\{q_s^-\}$ and the other for $\{p_r^-\}$:

$$\sum_{j=0}^{K} c_{s-j}\, q_j^- = 0 \; (0 \leq s \leq K, q_0^- = 1), \quad p_r^- = \sum_{j=0}^{r} c_{r-j} q_j^- \; (0 \leq r \leq K). \tag{9}$$

After the set $\{q_s^-\}$ is extracted from the input data $\{c_n\} (0 \leq n \leq N-1)$, the other set $\{p_r^-\}$ becomes immediately available via the analytical expression $p_r^- = \sum_{j=0}^{r} c_{r-j} q_j^- (0 \leq r \leq K)$ from (9). Thus, in fact, the set $\{p_r^-, q_s^-\}$ is obtained by solving only one system of linear equations (that for $\{q_s^-\}$). Earlier, when discussing pole-zero coincidences, it was stated that this comes from correlation between the numerator $(P_{K'})$ and the denominator $(Q_{K'})$ polynomials in the Padé quotient $P_{K'}/Q_{K'}$. This correlation is evidenced by Eq. (9) where the expansion coefficients $\{p_r^-\}$ of $P_{K'}$ are derived from the expansion coefficients $\{q_s^-\}$ of $Q_{K'}$.

To extract the peak parameters, the characteristic equation $Q_K^-(z^{-1}) = 0$ is solved, leading to K unique roots $z_{k,Q}^{-1} = \mathrm{e}^{-i\tau\omega_{k,Q}^-} (1 \leq k \leq K)$. Thus, the sought eigenfrequency $\omega_{k,Q}^-$ is deduced via $\omega_{k,Q}^- = (i/\tau) \ln(z_{k,Q}^{-1})$. As before, $z_{k,P}^{-1}$ and $z_{k,Q}^{-1}$ denote the zeros of $P_K^-(z^{-1})$ and $Q_K^-(z^{-1})$, respectively. The zeros $z_{k,Q}^{-1}$ are required for quantification. In addition, for signal–noise separation via Froissart doublets the zeros $z_{k,P}^{-1}$ are also needed.

Via the FPT$^{(-)}$, the parameters $\{\omega_{k,Q}^{-}, d_k^{-}\}$ $(1 \leq k \leq K)$ of each physical resonance are obtained directly from the examined MRS time signal. The k^{th} metabolite concentration is computed from the reconstructed amplitudes $|d_k^{-}|$ as $\mathrm{C}_{\text{met}}^{-} = (25\mu\text{M/g})|d_k^{-}|$ of ww of the scanned tissue.

2.2 Noise corruption of the input data

Reconstructions were performed using the input data that were corrupted by noise. The latter were created by adding complex-valued random zero-mean Gauss-distributed white noise of certain levels to the noiseless MRS time signal. The selected noise levels were $\sigma = 0.00289\,\text{RMS}$ and $\sigma = 0.0289\,\text{RMS}$, with RMS being the root-mean-square of the noise-free time signal, as noted. We use RMS as a quantifier of noise because this parameter reduces both the bias relative to the actual (sought) value as well as the variance of noise. The RMS is a measure of the signal dynamics, and converts signal oscillations to variations of the power of the signal across the given bandwidth [34].

There are many sources of noise that can arise in association with encoding MRS time signals. Among these are thermal Brownian random motion of water and other molecules related to the electronic circuitry, as well as respiratory motion, eventually peristalsis etc., depending upon the part of the patient's body for which the encoding is carried out. Moreover, when encoding is performed on clinical (1.5 T) scanners, the SNR is lower compared to higher field scanners. Notably, Brownian motion entails enormous molecular scattering. Therefore, this corresponds to the theorem of large numbers, leading to a Gaussian distribution. Consequently, random noise can be imitated by Gaussian distributed white noise. Since random noise in the encoded MRS time signals is distributed across all the frequencies in a given bandwidth, it is, de facto, white Gaussian noise. Therefore, the time signals corrupted with Gaussian white noise are "a mathematical phantom" for the corresponding MRS free induction decay curves.

2.3 Non-parametric signal processing via the FPT and the FFT

The Padé and Fourier spectra can only be compared with regard to total shape spectra since, as a non-parametric estimator, that is all the FFT can compute. The Fourier spectrum is given by:

$$F_k = \frac{1}{N}\sum_{n=0}^{N-1} c_n \exp(-2i\pi kn/N); \quad 1 \leq k \leq N-1, \tag{10}$$

where $2\pi k/T$ are fixed Fourier grid frequencies that are unrelated to ω_k from c_n. Here, T is the total duration or acquisition time of the signal, $T = N\tau$. The variable $\exp(-2i\pi kn/N)$ in (10) is an undamped harmonic.

The non-parametric data are provided by the FPT as soon as the Padé polynomials P_K^{-} and Q_K^{-} are extracted from the time signal $\{c_n\}$. The ratio P_K^{-}/Q_K^{-} is the complex-valued total shape spectrum, or envelope, whose real part is the absorption spectrum,

whereas its imaginary part is the dispersion spectrum. Note that the non-parametric FPT directly generates the total shape spectrum P_K^-/Q_K^- at any given set of sweep frequencies, and these need not correspond to the preassigned Fourier grid [72,73,77]. In other words, the FPT can interpolate, according to the actual features of the analyzed time signal.

2.4 Quantification of MRS time signals from breast fibroadenoma by the FPT: parametric signal processing

The FPT quantifies MRS data via polynomial rooting. This is a single numerical procedure whereby the roots of the characteristic equations of the numerator (P_K) and the denominator (Q_K) polynomials generate the zeros and poles of the Padé spectrum P_K^-/Q_K^-. Since the rational function P_K^-/Q_K^- is a meromorphic function, the zeros of Q_K^- are the poles of P_K^-/Q_K^-. Recall that meromorphic functions are functions whose only singularities are poles. Roots $z_{k,Q}^{-1}$ of equation $Q_K^-\left(z^{-1}\right)=0$ reconstruct the fundamental or eigen-frequencies $\omega_{k,Q}^-$. The amplitude d_k^- is given via the analytical expression for the Cauchy residue of $P_K^-(z^{-1})/Q_K^-(z^{-1})$ taken at the k^{th} pole $z^{-1}=z_{k,Q}^{-1}$ as per Eq. (3).

Consequently, since the quantification problem entails finding the eigen-set $\{\omega_{k,Q}^-, d_k^-\}$ $(1\le k\le K)$, it might be presumed that this is the concluding part of spectral analysis. This is not the case, however, since this segment of the analysis does not, in fact, generate the eigenset $\{\omega_{k,Q}^-, d_k^-\}$ $(1\le k\le K)$ with K being the true number of resonances. Instead, since, as mentioned, an over-determined system of linear equations is set up, a larger collection is produced $\{\omega_{k,Q}^-, d_k^-\}$ $(1\le k\le K')$, with K' as the sum of K genuine resonances and K'' spurious resonances $(K'=K+K'')$. In other words, we obtain $P_{K'}^-/Q_{K'}^-$ instead of P_K^-/Q_K^-.

In order to omit the K'' false (noisy or noise-like) resonances that are not the constituents of the K input eigen-frequencies and the K associated eigen-amplitudes, it is necessary to root the numerator polynomial via $P_{K'}^-\left(z^{-1}\right)=0$, giving the zeros $\left\{z_{k,P}^{-1}\right\}$ $(1\le k\le K')$ of the spectrum $P_{K'}^-\left(z^{-1}\right)/Q_{K'}^-\left(z^{-1}\right)$. Via the stability assessment within signal–noise separation, or SNS, binning is carried out according to stable versus unstable resonances as a function of the varying degree K' of polynomials $P_{K'}^-$ and $Q_{K'}^-$. Note that the expansion coefficients $\{p_r^-\}$ of $P_{K'}^-$ are given analytically as a linear combination of the expansion coefficients $\{q_s^-\}$ of $Q_{K'}^-$ as per (9).

3 Results

The constancy of the spectral parameters was checked by systematically increasing the signal length for the same bandwidth (i.e. three acquisition times). The reconstructed spectral parameters are shown in Table 2 at total orders $K=350$, 850 and 1024. For the total signal length $N=2048$, the partial signal length N_{P} is given by $N_{\text{P}}=2K$.

In the top panel (i) of Table 2, at $K=350$, i.e. at $N_{\text{P}}=700$, only eight of the nine genuine resonances were reconstructed. In the chemical shift interval from

Table 2 Reconstructed spectral parameters and metabolite concentrations by using the fast Padé transform, or FPT$^{(-)}$, for fibroadenomatous breast

n_k or #	Re(ν_k^-) (ppm)	Im(ν_k^-) (ppm)	$\lvert d_k^- \rvert$ (au)	C_k^- (μM/g)	M_k^-
(i) Padé-reconstructed data: $N_P = 700$, $N = 2048$ (PC, PE: unresolved)					
1	1.332	0.0008	0.059	1.475	LAC
2	1.471	0.0008	0.004	0.100	ALA
3	3.212	0.0008	0.002	0.050	CHO
5	3.221	0.0009	0.022	0.550	PE
6	3.232	0.0008	0.003	0.075	GPC
7	3.251	0.0008	0.039	0.975	β-GLC
8	3.273	0.0008	0.014	0.350	TAU
9	3.281	0.0008	0.019	0.475	M-INS
(ii) Padé-reconstructed data: $N_P = 1700$, $N = 2048$ (Fully converged)					
1	1.332	0.0008	0.059	1.475	LAC
2	1.471	0.0008	0.004	0.100	ALA
3	3.212	0.0008	0.002	0.050	CHO
4	3.220	0.0008	0.003	0.075	PC
5	3.221	0.0009	0.019	0.475	PE
6	3.232	0.0008	0.003	0.075	GPC
7	3.251	0.0008	0.039	0.975	β-GLC
8	3.273	0.0008	0.014	0.350	TAU
9	3.281	0.0008	0.019	0.475	M-INS
(iii) Padé-reconstructed data: $N_P = 2048 = N$ (Fully converged)					
1	1.332	0.0008	0.059	1.475	LAC
2	1.471	0.0008	0.004	0.100	ALA
3	3.212	0.0008	0.002	0.050	CHO
4	3.220	0.0008	0.003	0.075	PC
5	3.221	0.0009	0.019	0.475	PE
6	3.232	0.0008	0.003	0.075	GPC
7	3.251	0.0008	0.039	0.975	β-GLC
8	3.273	0.0008	0.014	0.350	TAU
9	3.281	0.0008	0.019	0.475	M-INS

The input spectral parameters are taken from Table 1 to create the noise-free time signal. These data were then corrupted by adding zero-mean random complex-valued Gaussian noise of a level equal to 0.0289 multiplied by the root mean square or RMS of the noise-free time signal. At partial signal lengths $N_P = 700$ and 1700 and at full signal length $N = 2048$ the computations were carried out as shown on panels (i), (ii) and (iii), respectively. Panels (ii) and (iii) show full convergence

3.220 to 3.221 ppm there should have been two resonances reconstructed. However, only one resonance was generated, at 3.221 ppm. Phosphocholine, PC, peak #4 was not seen. Since the peak height of phosphoethanolamine, PE, was overestimated, the computed PE concentration was 0.075μM/g greater than its actual value. The spectral parameters and concentrations of the other seven metabolites were correct

at $N_P = 700$. At $N_P = 1700$ convergence was attained as seen on the middle panel (ii) of Table 2. At all higher partial signal lengths, as well as at full signal length N convergence remained stable. The stability of convergence is illustrated in the bottom panel (iii) of Table 2 at full signal length $N = 2048$, where all the reconstructed parameters are identical to those in panel (ii), as well as to the input data presented in Table 1.

In the FFT, the signal length is given by a composed number 2^m ($m = 1, 2, \ldots$) and specifically for $N = 2048$, we have $N = 2^{11}$. Since this restriction is unnecessary for the FPT, we chose arbitrary truncation levels of N as $N_P = 700$ and 1700, neither of which is of the form 2^m necessitated by the FFT. In other words, in the FPT, the partial signal length N_P can be any positive integer less than or equal to N.

At the two partial signal lengths $N_P = 700$ and 1700 and at the full signal length $N = 2048$ on the top (i), middle (ii) and bottom (iii) panels of Fig. 1, respectively, with the noise level of $\sigma = 0.0289$ RMS metabolite maps for the Padé-reconstructed concentrations are presented. There are two independent sets of abscissae and ordinates on these maps, such that for metabolites ## 3 to 9, namely choline (3.212 ppm) to myoinositol (3.281 ppm), the abscissae and ordinates are on the bottom and left, respectively. For metabolites ## 1 and 2, i.e. lactate (1.332 ppm) and alanine (1.471 ppm) that are far from the others, the abscissae and ordinates are on the top and right, respectively.

At $N_P = 700$ [top panel (i) of Fig. 1], the exact input data for PC, phosphocholine and PE, phosphoethanolamine, and the Padé-reconstructed data are not in accord. Namely, the metabolite concentration is only generated for a single resonance at 3.221 ppm. This concentration is equal to the sum of the actual concentrations of PC + PE. For the other seven metabolites, the computed concentrations are correct at $N_P = 700$. This is shown numerically and by the confluence of the symbols $\times$ and the open circles (o). The Padé-reconstructed chemical shifts and concentrations exactly coincide with the input data for all nine metabolites at $N_P = 1700$, as shown on the middle panel (ii) of Fig. 1. For the total signal length $N = 2048$, as depicted on the bottom panel (iii) of Fig. 1, the metabolite concentration map completely matches that of panel (ii). The stable convergence within the FPT is further seen thereby.

The Padé-reconstructed absorption component shape spectra and the total shape spectra for the interval between 3.2 and 3.3 ppm are presented in Fig. 2 at the partial signal lengths $N_P = 700$ and $N_P = 1700$ as well as for the total signal length $N = 2048$ for breast fibroadenoma data with the noise level of $\sigma = 0.0289$ RMS . At $N_P = 700$, the absorption total shape spectrum is nearly converged, as shown on the top right panel (iv). However, the structure of the almost converged peak "4+5" on the total shape spectrum does not in any way indicate that two peaks should be found therein. On the component shape spectrum [upper left panel (i)], however, the lack of convergence is clear since only one peak (#5, PE) appears at 3.221 ppm and peak #4, PC is not resolved. On the left middle panel (ii) of Fig. 2 at $N_P = 1700$, the component shape spectrum is converged: peaks ## 4 and 5 are resolved, with their correct heights, as is the case for all the other resonances. Phosphocholine completely underlies PE, therein. Still however the total shape spectrum gives no indication of this, since the fully converged peak 4 + 5 has a perfect Lorentzian shape [panel (v)]. For both the

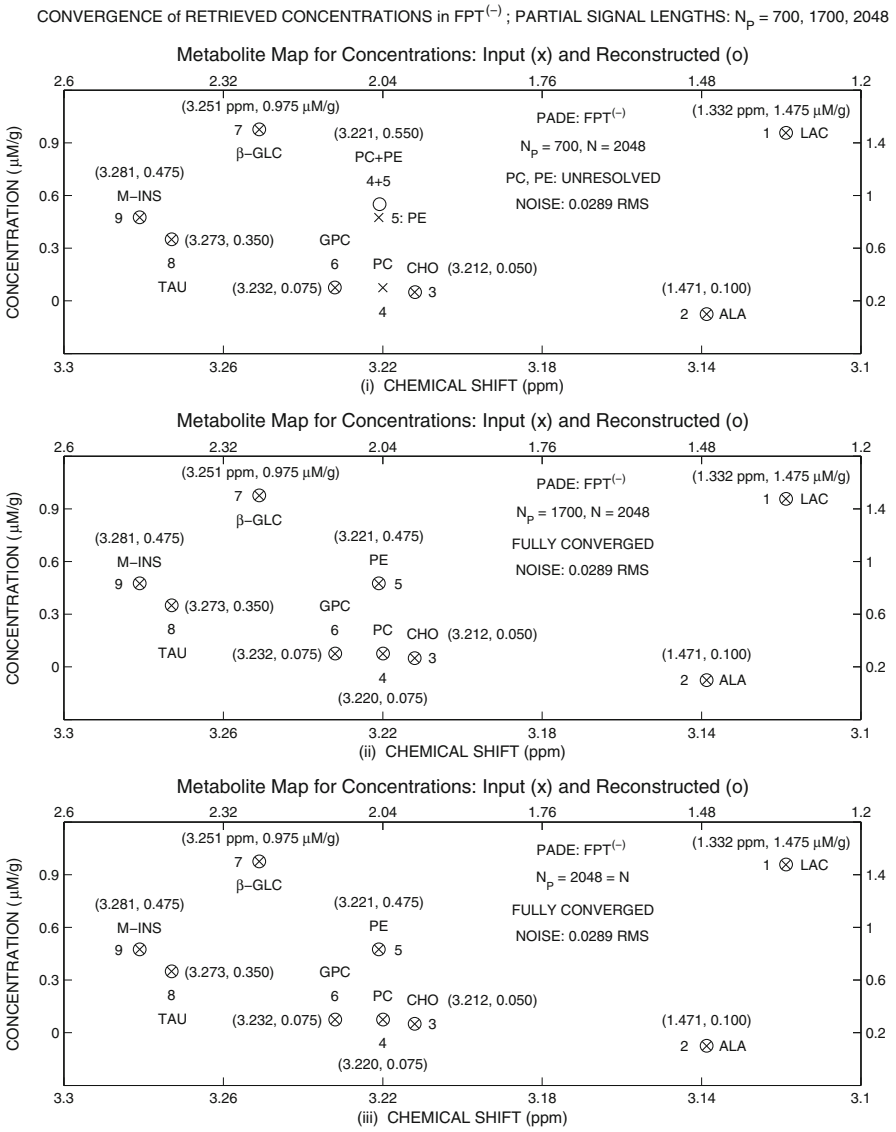

Fig. 1 Concentration map of metabolites at two partial signal lengths $N_{\mathrm{P}} = 700$ and 1700 as well as at full signal length $N = 2048$ on (i), (ii) and (iii), respectively, as reconstructed via the fast Padé transform $\mathrm{FPT}^{(-)}$ for the noisy time signal $c_n + w_n$, based on Ref. [67]. Here, $\{c_n\}(0 \le n \le N-1)$ is the noiseless time signal sampled from Eq. (5), using the fundamental frequencies and amplitudes $\{\nu_k, d_k\}(0 \le k \le K)$ listed in Table 1 for $K = 9$. The set $\{w_n\}(0 \le n \le N-1)$ is the additive random zero-mean Gaussian white noise of standard deviation σ, where $\sigma = 0.0289$ RMS with RMS being the root-mean-square of the noiseless time signal $\{c_n\}$. The ordinates are metabolite concentrations in micromole per gram (μM/g) of tissue wet weight, or ww, and the abscissae are dimensionless frequencies as chemical shifts in parts per million, or ppm. Two sets of abscissae and ordinates are shown: *top* and *right* ## 1, 2 (Lactate *LAC*, Alanine *ALA*) and *bottom* and *left* ## 3-9 (Choline *CHO*,. . ., Myoinositol *M-INS*). The full list of metabolites' acronyms is given in "Abbreviations"

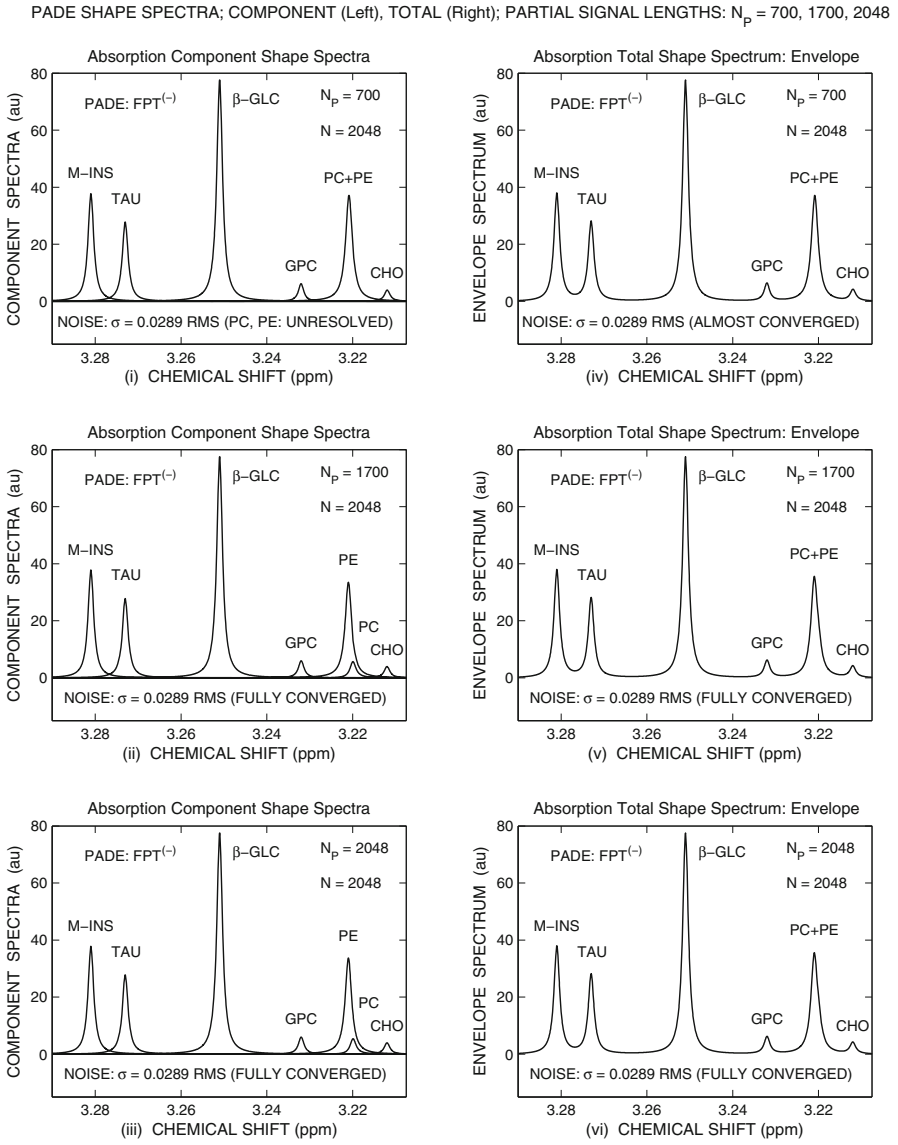

Fig. 2 Padé-reconstructed absorption spectra within the frequency range of 3.2–3.3 ppm for fibroadenomatous breast for the noisy time signal sampled from Eq. (5) with the parameters from Table 1 based on Ref. [67]. Component shape spectra: left panels (i)–(iii) and total shape spectra: right panels (iv)–(vi). On (iv) at the partial signal length $N_{\mathrm{P}} = 700$, the total shape spectrum is almost, but not yet fully converged. The corresponding component spectrum on (i) did not resolve peak # 4 (PC) and overestimated peak # 5 (PE). The component spectra on (ii) is converged at $N_{\mathrm{P}} = 1700$; as is the total shape spectrum on (v). The two resonances PC (# 4: 3.220 ppm) and PE (# 5: 3.221 ppm) are correctly detected on (ii), even though PC completely underlies PE. The difference between the envelopes on (iv) and (v), i.e. the residual is buried in the background noise. At all longer partial as well as signal lengths, convergence of the absorption component and total shape spectra remain stable, as illustrated on the bottom panels (iii) and (vi) for $N = 2048$

absorption component shape spectrum and the total shape spectrum, convergence is stable at longer partial signal lengths, as well as for the full signal length. An illustration of this stable convergence is provided at full signal length $N = 2048$, in the bottom panels of Fig. 2. Moreover, the so-called residual spectra [computed as the difference between any two pairs of envelopes from panels (iv) to (vi)] are buried in the background noise. This shows that the residual spectra are insufficient for judging the overall quality of reconstruction. In the "FFT + fitting" approaches, the residual spectra (model-input data) are overwhelmingly used as one of the main criteria (the so-called figure of merit) for validating least square estimations.

A succinct, yet comprehensive summary of key clinical MRS data for breast fibroadenoma is provided in Fig. 3. In panel (i) with the input data, the real part (Re) of the complex time signal is shown, as per the encoded data from breast fibroadenoma reported in Ref. [67], with added Gaussian-distributed noise at $\sigma = 0.0289$ RMS. To avoid clutter, the imaginary part (Im) of the FID, which is similar, is not shown herein. The full signal length is $N = 2048$. All the output data are shown either for the interval between 3.2 ppm and 3.3 ppm or [3.16, 3.34] ppm. In panels (ii), (iii), (iv) depicted are the output data as spectra. Metabolite concentrations are displayed in panel (v). Signal–noise separation is then illustrated in panels (vi) and (vii) for FWHMax (full width at half maximum: spectral poles) equals FWHMin (full width at half minimum: spectral dips) for non-physical data. The distinction between true and spurious peak heights is shown in panel (viii).

The absorption total shape spectrum as reconstructed via the fast Fourier transform, FFT, is presented in panel (ii) at full signal length ($N = 2048$). It is seen therein that the Fourier-reconstructed envelope or total shape spectrum is completely inaccurate, revealing only a few rough, stunted broad peaks that are not at all clinically useful. There is not even a hint of the presence of a choline peak #3 or a glycerophosphocholine peak #6, by inspection along the irregular sinc-like baseline.

The FFT-reconstructed total shape spectrum is sharply contrasted with that of the FPT which fully converged at partial signal length $N_P = 1700$ on panel (iii). The component shape spectra is also fully converged in the FPT at $N_P = 1700$ on panel (iv). Thus phosphocholine, PC, is seen to completely underlie phosphoethanolamine, PE. Identification and quantification of this underlying PC peak is totally impossible with the FFT and post-processing fitting. To match the FPT in (iii) associated with a time signal sampled at $N = 2048$ (2 kilobytes). the FFT requires $N = 65536$, (64 kilobytes) signal points in a single encoding and consequently there is a 32-fold lengthening of each transient in the Fourier analysis.

The converged concentration map at $N_P = 1700$ is displayed on the top right panel (v), wherein the concentrations of all the metabolites, including PC are accurately computed. Panels (vi) and (vii) identify spurious data via: FWHMax = FWHMin, symbolized as ⊙ (confluence of O and •) specifying Froissart doublets. There is marked instability for two noise levels differing by a factor of 10 on panel (vi) ($\sigma = 0.00289$ RMS) and panel (vii) ($\sigma = 0.0289$ RMS). The zero peak heights in (viii), indicating that the abscissa crosses the centers of the empty circles, represent the third "signature" of spurious resonances.

Another threefold signature identifies true resonances, namely: FWHMax $\neq$ FWHMin with coincidence of the reconstructed and input poles (O and $\times$) as indi-

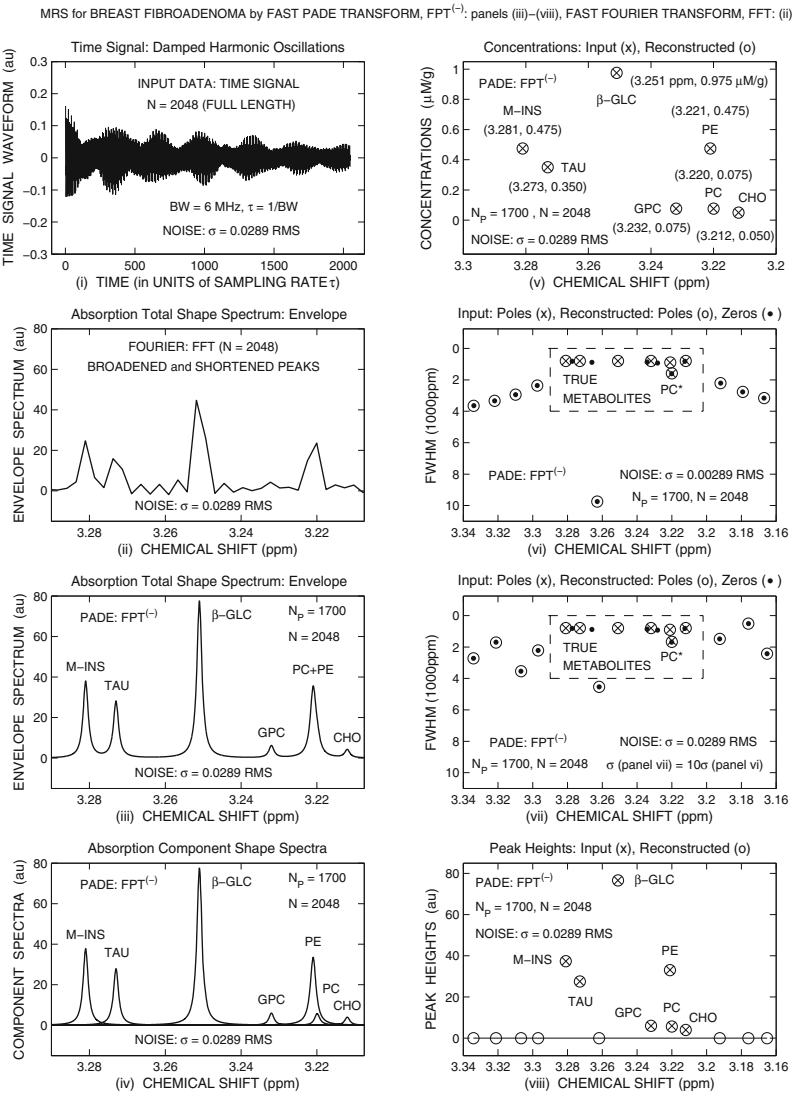

Fig. 3 A comprehensive summary of MRS for this breast fibroadenoma data. Time signal panel (i) is the real part of the input data $\{c_n\}(0 \le n \le N-1)$ from Eq. (5), based on Table 1 and Ref. [67]. Larmor frequency (ν_L) is 600 MHz, bandwidth (BW) is 6 MHz and its reciprocal is the sampling rate τ. The output data are shown for the two intervals between 3.2 ppm and 3.3 ppm and within [3.16, 3.34] ppm. Total shape spectra are on panel (ii) for the fast Fourier transform, or FFT, with no convergence at $N_P = 2048$ and on (iii) for the fast Padé transform, or FPT with convergence at $N_P = 1700$. (iv) Component shape spectrum in the FPT$^{(-)}$ converged at $N_P = 1700$. (v) Metabolite concentration map reconstructed by the FPT$^{(-)}$. The *symbols* used in (v) through (viii) are as follows: input data ($\times$) and output data (O, $\bullet$). To facilitate visualization, the FWHM is doubled at 3.220 ppm for PC and this is indicated by PC* in (vi) and (vii). Signal–noise separation, or SNS, shown in (vi)–(viii). (vi), (vii) The true metabolites inside the *dashed box* are stable at two noise levels differing by a factor of 10, notwithstanding occasional proximity of their poles and zeros. The non-physical resonances (outside the box) are unstable at the two different noise levels as well as showing complete pole-zero coincidence. (viii) Physical resonances have non-zero heights, while those that are non-physical have zero heights

cated by ⊗ together with robust stability against the two noise levels differing by 10 in panels (vi) and (vii) as well as non-zero peak heights in panel (viii). Although these true structures may also display pole-zero near-coincidences as FWHMax ≈ FWHMin, and their peak heights may be close to zero, genuine resonances remain completely unchanged for different noise levels, as seen in the panels (vi) and (vii), within the dash-lined box. Notably, noise does not enter this latter box in which most of the densely spaced genuine poles (o) and zeros reside. Conversely, one genuine zero associated with PE is not seen in panels (vi) and (vii), since it lies outside the windowed FWHM. Its large FWHMin produces a long pole-zero distance which secures stability of PE, in face of the small difference of 0.001 ppm between the chemical shifts of PE and its very close neighbor PC.

Overall, via the Padé-reconstructed parameters in MRS reconstructed by the FPT, namely the peak heights in panel (viii) multiplied by FWHMax in panel (vi) or (vii), the metabolite concentrations in panel (v) can be directly deduced. This is the diagnostically most vital information. Via the fast Padé transform, SNR can be further improved and total acquisition time shortened, using barely a quarter of the 128 transients needed for convergence in FFT [67]. This provides major advantages for MRS via FPT: improved accuracy via better clinical reliability and higher efficiency through shorter examination time for the patient.

4 Discussion

4.1 The algorithmic success of the FPT for MRS time signals

The success of the fast Padé transform derives, within theory as well as in practice, directly from quantum mechanics, which is well-recognized as the most adequate physics theory. In a manner equivalent to that by which quantum physics prescribes the particular form (5) of a sum of damped harmonics for the free induction decay curve in the time domain, the same theory gives, as well, the frequency spectrum by the unique ratio of two polynomials, as in the fast Padé transform. The arguments expounded in Refs. [72,73] explain in detail how this comes about. In the present paper, we see how this algorithmic success directly translates into the potential to solve a critical public health problem within the domain of timely cancer diagnostics through magnetic resonance spectroscopy.

4.1.1 The resolution capabilities of the FPT versus the FFT for noise corrupted MRS time signals

In our previous work applying the FPT to the noiseless MRS data from breast cancer, fibroadenoma and normal breast [10,72,83], given that our focus was resolution and quantification of the overlapping components, we chose not to include a comparison with the FFT. In the present study, however, we decided to directly compare the performance of conventional Fourier processing with the fast Padé transform for MRS using breast fibroadenoma data. This decision was based upon the large and rapidly expanding number of publications on MRS of benign and cancerous breast lesions, all

based upon total choline assessments using standard Fourier processing. The fact that these Fourier-based data have yielded only a limited, incremental success particularly highlights the need for such comparisons. Clearly, such comparisons can only be made for resolution of the total shape spectrum, which is all that the FFT can provide, as mentioned.

The reasons for the dramatically improved resolution with the FPT are multi-fold. With regard to interpolation, it should be first recalled that the Padé grid differs fundamentally in the frequency domain from the Fourier grid. The absorption spectra in the FPT$^{(-)}$ is given by the real parts of the complex-valued polynomial quotients $P_K^-(z^{-1})/Q_K^-(z^{-1})$, where $z^{-1} = e^{-i\omega\tau}$ can be taken at any frequency ω i.e. the sweep frequency. Consequently, the Padé grid is just an arbitrary mesh for plotting the frequency ω and can be selected completely independently of the number of signal points $\{c_n\}$ used. Thus, the FPT achieves interpolation in spectra, based on the actual analyzed time signal. In complete contradistinction, the minimal separation $\omega_{\min}$ in a spectrum from the FFT is determined by the total acquisition time T. As noted, the FFT spectrum is defined only on the Fourier grid points $\omega_k = 2\pi k/T$ $(k = 0, 1, 2, 3, \ldots, N-1)$, where N is the total signal length. Consequently, the FFT cannot interpolate. Instead, a surrogate procedure is customarily done by the sinc-type interpolation in the frequency domain as a direct result of the zero-filling in the time domain. The net effect is that undulations become superimposed on the rolling background and, sometimes, the visual appearance of the spectrum is thereby superficially improved. Since superfluous data (zeros) are added in the encoding domain, zero-padding of the time signal does not, in fact, improve resolution in the Fourier spectrum.

The FPT also has powerful extrapolation capabilities. The polynomial quotient P_K^-/Q_K^- is an extrapolator because the inverse of Q_K^- is an infinite sum (Maclaurin series). Moreover, upon convergence, the FPT can extend the input set $\{c_n\}$ $(0 \leq n \leq N-1)$ to any $N' > N$. This extrapolation beyond the N input signal points is achieved by predicting the non-encoded set $\{c_n\}$ $(n = N, N+1, \ldots)$ using the extracted prediction coefficients $\{q_s^-\}$ $(0 \leq s \leq K)$ from Eq. (9). It is in this way that the FPT can provide reliable inference about the unmeasured time signal beyond the total acquisition time T. In other words, Padé spectra inherently contain inferences on the otherwise unmeasurable infinitely long time signals by relying solely upon the corresponding encoded data of finite lengths [72,73,77]. These extrapolation capabilities of the FPT contribute substantially, as well, to resolution enhancement. Due to its non-linearity, as is apparent from the polynomial quotient for the spectrum, the FPT can effectively reduce noise, also further improving resolution. As a ratio of two polynomials, an extra degree of freedom is provided to cancel out noise from the numerator P_K^- and the denominator Q_K^-, whereas in the FFT as a single polynomial and being linear, noise is imported intact from the measured time domain [72,73,77].

The results presented in this paper demonstrate the superior capabilities of the FPT for these noise corrupted MRS time signals from the breast. The practical clinical implications of this capability will be discussed in the next subsection.

4.2 Clinical implications of these findings

4.2.1 Padé-optimized MRS for enhanced breast cancer diagnostics

Superior resolution: shortened examination time for the patient. Based on the superior resolution performance of the FPT compared to the FFT for MRS time signals from ovarian cancer [34], we recently discussed in detail, how this would change the approach to MRS data acquisition, by encoding fewer and relatively short MRS time signals. The direct practical implications are shortened examination time, thereby diminishing costs of the MRS procedure, and providing a more comfortable setting for the patient.

The results presented in this paper suggest that similar advantages would be possible for Padé-optimized MRS examinations of the breast. In addition, in light of the often needed volumetric coverage in breast diagnostics, the higher resolution of the FPT for MRS becomes even more critical for MRSI. This is because spectroscopic imaging measurements coupled with 3-dimensional spatial resolution need to be performed within a reasonable total acquisition time in order to be clinically practical.

As reviewed earlier in this paper, attempts have been made to improve resolution and SNR of MRS spectra from the breast via higher magnetic field scanners [52,55–59]. Of course, such recorded MRS time signals would thereby contain less noise compared to 1.5 T clinical scanners. Nevertheless, the sought degree of accuracy in determining whether or not a breast lesion is cancerous was not accomplished thereby [56]. Furthermore, the high cost of such examinations would preclude the very goal of more widespread use of MRS in breast cancer diagnostics.

Beyond "total choline": possibilities to assess more specific breast cancer markers. Via Fourier processing for proton MRS, a converged total shape spectrum such as panel (iii) of Fig. 3 under ideal encoding conditions (high magnetic field strength, state-of-the-art coil design, meticulous attention to shimming and other technical or "hardware" aspects), within e.g. the chemical shift region of interest, 3.2–3.3 ppm, would be the maximum that could be provided. Based upon the total shape spectrum seen on panel (iii) of Fig. 3, it would be impossible to even know that phosphocholine lies therein, i.e. that there is a PC peak beneath phosphoethanolamine, let alone to determine the actual concentration of PC.

Attempts have been made to use in vivo ^{31}P MRS in order to assess the components of total choline which thereby appear as closely-lying though isolated resonances [100]. However, since the gyromagnetic ratio for ^{31}P is nearly 2.5 times lower than that for proton hydrogen and also since phosphorus is far less abundant, a much higher magnetic field strength is needed (7T). Another disadvantage from a practical point of view is that that unlike proton MRS which can be performed with the same equipment as standard MRI, for ^{31}P MRS a second radiofrequency subsystem would be required.

As reported in Refs. [10,72,83], the FPT unequivocally identified and exactly computed the concentration of phosphocholine, as well as the other metabolites in the spectra of normal breast, fibroadenoma and breast cancer, based on the data of Ref. [67] without added noise. Herein, the FPT succeeds in this task for noise-corrupted fibroadenoma data.

For the noiseless problems as reported in Refs. [10,72,83], convergence was achieved at a partial signal length $N_P = 1500$, such that 741 spurious resonances were also generated. In the presence of noise, the partial signal length needed for convergence was a bit longer ($N_P = 1700$). Consequently, some 841 in total or 100 more spurious resonances appeared than in the noiseless case. All facets of the Padé-based signal–noise separation, or SNS, namely pole-zero coincidence, zero amplitude and marked instability with change in noise level helped distinguish these numerous spurious resonances from the true metabolites. Notably, the amplitude of the true resonances, choline, GPC and PC were low, i.e. practically near zero. However, these resonances remained stable with a tenfold change in noise level [as seen in panels (vi) and (vii) of Fig. 3], such that these true metabolites could be reliably identified.

Thus, the genuine metabolites, no matter how closely overlapping (and that constitute only ∼1 % of the resonances that appeared in this breast fibroadenoma example) are definitively identified and precisely quantified via Padé-processing accompanied by the SNS. Especially in light of the results reported here, alongside our related and most recent study on breast cancer [101], fitting algorithms that are the current post-processing sequel to the Fourier-based reconstruction, are seen to be entirely unsuitable for MRS.

4.2.2 Some broader clinical perspectives: Padé-optimized MRS for personalized cancer medicine

The potential of Padé-optimized MRS lies in the possibility to monitor metabolism of a large number (25 or many more) metabolites, some of which may be cancer markers. Such information can then be correlated with the spatial localization of tumor. This can be applied not only for initial diagnostics, but also during and after therapy. With regard to the latter, the evaluated metabolic pathways can be correlated with the dose-response of tissue on molecular and cellular levels. Not only could early tumor detection be achieved thereby, but the possibilities for targeted therapies are also expanded. The obtained results can be used for further developments in drugs that disrupt specific metabolic pathways essential for tumour cell survival and proliferation. Introduction of such drugs into the clinic has already shown that patients vary widely in their responses. Advanced molecular imaging modalities such as MRS as well as positron-emission tomography (PET) combined with computerized tomography (CT) are likely to play a key role in predicting and detecting these responses. Innovations of this type can improve and guide treatment in individual patients in the spirit of truly personalized cancer medicine (PCM).

Optimized MRS for timely assessment or prediction of response to therapy for breast cancer. To date, there have been initial promising results using conventional Fourier-based MRS as well as diffusion weighted MRS to predict or assess breast cancer response to chemotherapy [102–104]. Most notably, a change in the assessed concentration of total choline at 24 h after the 1st dose of therapy appeared to predict clinical response to doxorubicin-based chemotherapy among fourteen patients with locally advanced breast cancer [102]. Recent data also suggest that radiation treatment in breast cancer might be enhanced via MRS and MRSI. Namely, tumor hypoxia, linked

to resistance to radiotherapy as well as to chemotherapy, is found to also be associated with regions of higher non-invasively assessed total choline, tCho, on MRSI in breast tumor models [105]. The authors of Ref. [105] report that via the FFT-type conventional data processing methods, the components of tCho could not be assessed. They note, however, that the increase in tCho under hypoxia was primarily due to elevated phosphocholine levels as shown by in vitro MRS. Taken together, these observations strongly suggest that we have only begun to "scratch the surface" of the possibilities for enhancing a more individualized approach to breast cancer treatment via MRS and MRSI, with Padé-optimization poised to play a pivotal role therein.

Dynamic MRS. The majority of research to date has been within steady-state MRS and MRSI, where metabolite concentrations are stationary or time-independent. However, MRS and MRSI can be also applied dynamically, to follow the time evolution of metabolite concentrations after intravenous injection of hyperpolarized biomarkers that can catalyze to cancer markers such as choline, lactate, etc. Early identification of responders versus non-responders to treatment can also be accomplished thereby. Very soon after administration of the relevant drug, assessment of metabolic uptake can reveal whether or not the patient is responding to the treatment. This information could facilitate appropriate subdivision of early responders versus non-responders and for whom prompt switching of therapy would be indicated.

Not only steady-state but also dynamic MRS could become cost-effective through mathematical optimization of data analysis via signal processing. In therapy, together with the expected improvement in patient outcome, dynamic MRS is also expected to improve cost-effectiveness by early detection (within days or even hours) of responders versus non-responders to the administered drug[1]. Besides the most crucial benefit for the patient, such advantages could translate into dramatic cost reduction. However, as is the case for steady-state MRS and MRSI, optimization of data analysis is vital. Thus far, most investigations using dynamic MRS also employ the "FFT + fitting" approaches. The drawbacks seen for steady-state MRS apply to dynamic MRS, as well. The situation becomes even worse insofar as phenomenological techniques are used instead of models with mechanistic kinetics for dose-effect relationships. Here, the clinical reliability of dynamic MRS can be improved by an appropriate combination of the FPT with Michaelis-Menten saturation kinetics for enzyme catalysis in a mechanistic description of chemical reactions leading to products as cancer biomarkers [106–109].

5 Conclusions

We conclude that for the potential of magnetic resonance spectroscopy or MRS, and spectroscopic imaging, or MRSI, to be realized for breast cancer diagnostics, mathematical optimization through the fast Padé transform, or FPT will be of critical importance. Conventional Fourier-based spectral reconstruction with post-processing

[1] This should be compared to months, as is often needed for conventional follow-up of disease progression based on tumor size.

through fitting has not provided the needed accuracy of MRS and MRSI for distinguishing breast cancer from fibroadenoma or other benign lesions of the breast. This is not unexpected given that the fast Fourier transform is a non-parametric, low resolution processor and that non-unique fitting procedures cannot provide any certainty whatsoever about closely-overlapping resonances that are of critical importance in MR spectra from the breast. The high-resolution, quantification-equipped fast Padé transform, is a paradigm shift of proven validity for optimally accurate processing of generic time signals comprised of complex damped harmonics as encountered across interdisciplinary research fields and technologies. These capabilities of the FPT are clearly demonstrated in the present paper whereby in the presence of realistic noise levels, the FPT reliably distinguishes spurious resonances from true metabolites and exactly computes the concentrations of the latter, including phosphocholine, or PC. Practical implications are underscored in that the high resolution of the FPT alongside improvement in the signal to noise ratio, translates directly into shortened examination time for the patient. The multi-faceted signal–noise separation procedure provides certainty in the face of a greatly over-determined system of linear equations, that the genuine i.e. physical resonances are identified unequivocally and the metabolite concentrations precisely computed. The far more abundant spurious resonances are all identified as such through pole-zero cancellations, zero or near zero amplitudes and their marked instability against various levels of truncation and/or noise. Applying the fast Padé transform to time signals encoded in vivo from benign and cancerous breast therefore will be the key step for MRS to realize its potential to become a reliable, cost-effective method for breast cancer diagnostics.

Acknowledgments This work was supported by Cancerfonden, Radiumhemmets Research Fund and FoUU to which the authors are grateful.

References

1. D.M. Parkin, F. Bray, P. Pisani, Global cancer statistics. CA Cancer J. Clin. **55**, 74–108 (2005)
2. N. Perry, M. Broeders, C. de Wolf, S. Törnberg, R. Holland, L. von Karsa, European guidelines for quality assurance in breast cancer screening and diagnosis. Fourth edition-summary document. Ann. Oncol. **19**, 614–622 (2008)
3. S.A. Eccles, E.O. Aboagye, S. Ali, A.S. Anderson, J. Armes, F. Berditchevski, Critical research gaps and translational priorities for the successful prevention and treatment of breast cancer. Breast Cancer Res. **15**, R92 (2013)
4. M. Sant, C. Allemani, R. Capocaccia, T. Hakulinen, T. Aareleid, J.W. Coebergh, M.P. Coleman, P. Grosclaude, C. Martinez, J. Bell, J. Youngson, F. Berrino, Stage at diagnosis is a key explanation of differences in breast cancer survival across Europe. Int. J. Cancer **106**, 416–422 (2003)
5. K. Armstrong, E. Moye, S. Williams, J. Berlin, E. Reynolds, Screening mammography in women 40 to 49 years of age: a systematic review for the American College of Physicians. Ann. Intern. Med. **146**, 516–526 (2007)
6. D. Saslow, C. Boetes, W. Burke, S. Harms, M.O. Leach, C.D. Lehman, E. Morris, E. Pisano, M. Schnall, S. Sener, R.A. Smith, E. Warner, M. Yaffe, K.S. Andrews, C.A. Russell, American Cancer Society Breast Cancer Advisory Group, American Cancer Society guidelines for breast screening with MRI as an adjunct to mammography. CA Cancer J. Clin. **57**, 75–89 (2007)
7. K. Belkić, M. Cohen, M. Márquez, M. Mints, B. Wilczek, A.H. Berman, E. Castellanos, M. Castellanos, Screening of high-risk groups for breast and ovarian cancer in Europe: a focus on the Jewish population. Oncol. Rev. **4**, 233–267 (2010)

8. A.W. Kurian, A.R. Hartman, M.A. Mills, J.M. Ford, B.L. Daniel, S.K. Plevritis, Opinions of women with high inherited breast cancer risk about prophylactic mastectomy: an initial evaluation from a screening trial including magnetic resonance imaging and ductal lavage. Health Expect. **8**, 221–233 (2005)
9. A. Clements, B.J. Henderson, S. Tyndel, G. Evans, K. Brian, J. Austoker, E. Watson, Diagnosed with breast cancer while on a family history screening programme: an exploratory qualitative study. Eur. J. Cancer Care **17**, 245–252 (2007)
10. K. Belkić, Dž. Belkić, Possibilities for improved early breast cancer detection by Padé-optimized MRS. Isr. Med. Assoc. J. **13**, 236–243 (2011)
11. C. Biesheuvel, A. Barratt, K. Howard, N. Houssami, I. Irwig, Effects of study methods and biases on estimates of invasive breast cancer overdetection with mammography screening: a systematic review. Lancet **8**, 1129–1138 (2007)
12. T. Salz, J.T. DeFrank, N.T. Brewer, False positive mammograms in Europe: do they affect reattendance? Breast Cancer Res. Treat. **127**, 229–231 (2011)
13. A. Seigneurin, C. Exbrayat, J. Labarère, P. Delafosse, M. Colonna, Association between diagnostic work-up with subsequent attendance in a breast cancer screening program for false-positive cases. Breast Cancer Res. Treat. **127**, 221–228 (2011)
14. P. Fitzpatrick, P. Fleming, S. O'Neill, D. Kiernan, T. Mooney, False-positive mammographic screening: factors influencing re-attendance over a decade of screening. J. Med. Screen. **18**, 30–33 (2011)
15. G.J. Heyes, A.J. Mill, M.W. Charles, Mammography—oncogenicity at low doses. J. Radiol. Prot. **29**, A123–A132 (2009)
16. H. Kuni, I. Schmitz-Feuerhake, H. Dieckmann, Mammography screening—neglected aspects of radiation risks. Gesundheitswesen **65**, 443–446 (2003)
17. S. Schrading, C.K. Kuhl, Mammographic, US, and MR imaging phenotypes of familial breast cancer. Radiology **246**, 58–70 (2008)
18. S. Feig, Cost-Effectiveness of mammography, MRI, and ultrasonography for breast cancer screening. Radiol. Clin. N. Am. **48**, 879–891 (2010)
19. E. Venturini, C. Losio, P. Panizza, M. Grazia Rodighiero, I. Fedele, S. Tacchini, E. Schiani, S. Ravelli, G. Cristel, M. Panzeri, F. De Cobelli, A. Del Maschio, Tailored breast cancer screening program with microdose mammography, US and MR imaging: short-term results of a pilot study in 40–49 year-old women. Radiology **268**, 347–355 (2013)
20. M. Kriege, C. Brekelmans, C. Boetes, P.E. Besnard, H.M. Zonderland, I.M. Obdeijn, R.A. Maolin, T. Kok, H. Peterse, M. Tilanus-Linthorst, S. Muller, J. Oosterwijk, L. Beex, R. Tollenaar, H. de Konig, E. Rutgers, J. Klijn, Magnetic Resonance Imaging Screening Study Group, Efficacy of MRI and mammography for breast-cancer screening in women with a familial or genetic predisposition. N. Engl. J. Med. **351**, 427–437 (2004)
21. M.O. Leach, C.R. Boggis, A.K. Dixon, D.F. Easton, R.A. Eeles, D.G. Evans, F.J. Gilbert, I. Griebsch, R.J. Hoff, P. Kessar, S. Lakhani, S.S. Moss, A. Nerurkar, A. Padhani, L. Pointon, D. Thompson, R. Warren, MARIBS Study Group, Screening with magnetic resonance imaging and mammography of a UK population at high familial risk of breast cancer: a prospective multicentre cohort study (MARIBS). Lancet **365**, 1769–1778 (2005)
22. F. Sardanelli, F. Podo, F. Santoro, S. Manoukian, S. Bergonzi, G. Trecate, D. Vergnaghi, M. Federico, L. Cortesi, S. Corcione, S. Morassut, C. Di Maggio, A. Cilotti, L. Martincich, M. Calabrese, C. Zuiani, L. Preda, B. Bonanni, L. Carbonaro, A. Contegiacomo, P. Panizza, E. Di Cesare, A. Savarese, M. Crecco, D. Turchetti, M. Tonutti, P. Belli, A.D. Maschio, Multicenter surveillance of women at high genetic breast cancer risk using mammography, ultrasonography, and contrast-enhanced magnetic resonance imaging (the high breast cancer risk Italian 1 study): final results. Invest. Radiol. **46**, 94–105 (2011)
23. A. Iglesias, M. Arias, P. Santiago, M. Rodríguez, J. Mañas, C. Saborido, Benign breast lesions that simulate malignancy: magnetic resonance imaging with radiologic–pathologic correlation. Curr. Probl. Diagn. Radiol. **36**, 66–82 (2007)
24. S. Lipnick, X. Liu, J. Sayre, L.W. Bassett, N. De Bruhl, M.A. Thomas, Combined DCE-MRI and single-voxel 2D MRS for differentiation between benign and malignant breast lesions. NMR Biomed. **23**, 922–930 (2010)
25. K. Okamoto, Y. Kurihara, K. Imamura, Y. Kanemaki, Y. Nakajima, M. Fukuda, I. Maeda, Desmoid tumor of the breast: the role of proton magnetic resonance spectroscopy for a benign breast lesion mimicking a malignancy. Breast J. **14**, 376–378 (2008)

26. L. Bartella, S.B. Thakur, E.A. Morris, D.D. Dershaw, W. Huang, E. Chough, M.C. Cruz, L. Liberman, Enhancing nonmass lesions in the breast: evaluation with proton (1H) MR spectroscopy. Radiology **245**, 80–87 (2007)
27. L. Liberman, G. Mason, E.A. Morris, D.D. Dershaw, Does size matter? Positive predictive value of MRI-detected breast lesions as a function of lesion size. Am. J. Roentgenol. **186**, 426–430 (2006)
28. M.L. Essink-Bot, A.J. Rijnsburger, S. van Dooren, H.J. de Koning, C. Seynaeve, Women's acceptance of MRI in breast cancer surveillance because of a familial or genetic predisposition. Breast **15**, 673–676 (2006)
29. M. Robson, Breast cancer surveillance in women with hereditary risk due to BRCA1 or BRCA2 mutations. Clin. Breast Cancer **5**, 260–268 (2004)
30. W.A. Berg, J.D. Blume, A.M. Adams, R.A. Jong, R.G. Barr, D.E. Lehrer, E.D. Pisano, W.P. Evans, M.C. Mahoney, L. Hovanessian Larsen, G.J. Gabrielli, E.B. Mendelson, Reasons women at elevated risk of breast cancer refuse breast MR imaging screening: ACRIN 6666. Radiology **254**, 79–87 (2010)
31. J. Wilkinson, C. Appleton, J. Margenthaler, Utility of breast MRI for evaluation of residual disease following excisional biopsy. J. Surg. Res. **170**, 233–239 (2011)
32. J.H. Shin, H.Y. Choi, S.N. Lee, Y.J. Kim, Microinvasive ductal carcinoma arising within a fibroadenoma: a case report. Acta Radiol. **47**, 643–645 (2006)
33. A. Fatemi-Ardekani, C. Boylan, M.D. Noseworthy, Identification of breast calcification using magnetic resonance imaging. Med. Phys. **36**, 5429–5436 (2009)
34. Dž. Belkić, K. Belkić, Strategic steps for advanced molecular imaging with magnetic resonance-based diagnostic modalities. Technol. Cancer Res. Treat. (2013). doi:10.7785/tcrt.2012.500401
35. Dž. Belkić, K. Belkić, Molecular imaging in the framework of personalized cancer medicine. Isr. Med. Assoc. J **15**, 665–672 (2013)
36. A. Malayeri, R. El Khouli, A. Zaheer, M. Jacobs, C. Corona-Villalobos, I. Kamel, K. Macura, Principles and applications of diffusion-weighted imaging in cancer detection, staging, and treatment follow-up. RadioGraphics **31**, 1773–1791 (2011)
37. S. Sinha, U. Sinha, Recent advances in breast MRI and MRS. NMR Biomed. **22**, 3–16 (2009)
38. M. Tozaki, E. Fukuma, 1H MR spectroscopy and diffusion-weighted imaging of the breast: are they useful tools for characterizing breast lesions before biopsy? Am. J. Roentgenol. **193**, 840–849 (2009)
39. C.A. Corum, A.D. McIntosh, P.J. Bolan, M. Nelson, A.L. Snyder, N.J. Powell, J. Boyum, T.H. Emory, D. Yee, T.M. Tuttle, L.I. Everson, M. Garwood, Feasibility of single-voxel MRS measurement of apparent diffusion coefficient of water in breast tumors. Magn. Reson. Med. **61**, 1232–1237 (2009)
40. U. Sharma, R.G. Sah, R. Parshad, R. Sharma, V. Seenu, N.R. Jagannathan, Role of apparent diffusion coefficient values for the differentiation of viable and necrotic areas of breast cancer and its potential utility to guide voxel positioning for MRS in the absence of dynamic contrast-enhanced MRI data. Magn. Reson. Imaging **30**, 649–655 (2012)
41. R. Woodhams, K. Matsunaga, K. Iwabuchi, S. Kan, H. Hata, M. Kuranami, M. Watanabe, K. Hayakawa, Diffusion-weighted imaging of malignant breast tumors: the usefulness of apparent diffusion coefficient (ADC) value and ADC map for the detection of malignant breast tumors and evaluation of cancer extension. J. Comput. Assist. Tomogr. **29**, 644–649 (2005)
42. M. Descoteaux, C. Poupon, Diffusion-weighted MRI, in *Magnetic Resonance Imaging and Spectroscopy, Volume 3, Comprehensive Biomedical Physics*, ed. by Dž. Belkić, K. Belkić (Elsevier, Amsterdam, 2014), pp. 81–97
43. E. Eyal, M. Shapiro-Feinberg, E. Furman-Haran, D. Grobgeld, T. Golan, Y. Itzchak, R. Catane, M. Papa, H. Degani, Parametric diffusion tensor imaging of the breast. Invest. Radiol. **47**, 284–291 (2012)
44. N. Nissan, E. Furman-Haran, M. Shapiro-Feinberg, D. Grobgeld, H. Degani, Diffusion-tensor MR imaging of the breast: hormonal regulation. Radiology **271**, 672–680 (2014)
45. R. Katz-Brull, P.T. Lavin, R.E. Lenkinski, Clinical utility of MRS in characterizing breast lesions. J. Natl. Cancer Inst. **9**, 1197–1203 (2002)
46. G. Tse, D. Yeung, A. King, H. Cheung, W. Yang, In vivo MRS of breast lesions: an update. Breast Cancer Res. Treat. **104**, 249–255 (2007)
47. J.K. Begley, T.W. Redpath, F.J. Gilbert, In vivo proton MRS of breast cancer: a review of the literature. Breast Cancer Res. **14**, 207 (2012)
48. M.A. Jacobs, P.B. Barker, P.A. Bottomley, Z. Bhujwalla, D.A. Bluemke, Proton magnetic resonance spectroscopic imaging of human breast cancer: a preliminary study. J. Magn. Reson. Imaging **19**, 68–75 (2004)

49. P. Sijens, M. Dorrius, P. Kappert, P. Baron, R. Pijnappel, M. Oudkert, Quantitative multivoxel proton chemical shift imaging of the breast. Magn. Reson. Imaging **28**, 314–319 (2010)
50. C. Zhao, P. Bolan, M. Royce, N. Lakkadi, S. Eberhardt, L. Sillerud, S.-J. Lee, P. Posse, Quantitative mapping of total choline in health human breast using proton echo planar spectroscopic imaging (PEPSI) at 3 tesla. J. Magn. Reson. Imaging **36**, 1113–1123 (2012)
51. P.A. Balzter, M. Dietzel, Breast lesions: diagnosis by using proton MR spectroscopy at 1.5 and 3.0 T —systematic review and meta-analysis. Radiology **267**, 735–746 (2013)
52. I. Haddadin, A. McIntosh, S. Meisamy, C. Corum, A. Styczynski Snyder, N. Powell, M. Nelson, D. Yee, M. Garwood, P. Bolan, Metabolite quantification and high-field MRS in breast cancer. NMR Biomed. **22**, 65–76 (2009)
53. S. Gruber, B.K. Debski, K. Pinker, Three-dimensional proton MR spectroscopic imaging at 3 T for the differentiation of benign and malignant breast lesions. Radiology **261**, 752–761 (2011)
54. E. Kousi, I. Tsougos, K. Vasiou, Magnetic resonance spectroscopy of the breast at 3T: pre- and post-contrast evaluation for breast lesion characterization. Sci. World J. **2012**, 754380 (2012)
55. V.O. Boer, B.L. Bank, G. van Vliet, P. Luijten, D. Klomp, Direct B_0 field monitoring and read-time B_0 field updating in the human breast at 7 tesla. Magn. Reson. Med. **67**, 586–591 (2012)
56. P.J. Bolan, S. Meisamy, E. Baker, J. Lin, T. Emory, M. Nelson, L. Everson, D. Yee, M. Garwood, In vivo quantification of choline compounds in the breast with 1H MR spectroscopy. Magn. Reson. Med. **50**, 1134–1143 (2003)
57. I. Dimitrov, D. Douglas, J. Ren, N. Smith, A. Webb, A. Sherry, C. Malloy, In vivo determination of human breast fat composition by 1H magnetic resonance spectroscopy at 7T. Magn. Reson. Med **67**, 20–26 (2012)
58. D.W. Klomp, B. van de Bank, A. Raaijmakers, M. Korteweg, C. Possanzini, V. Boer, C. van de Berg, A. van de Bosch, P. Luijten, ^{31}P and ^{1}H MRS at 7T: initial results in human breast cancer. NMR Biomed. **24**, 1337–1342 (2011)
59. M. Korteweg, W. Weldhuis, F. Visser, P. Luijten, W. Mali, P. van Diest, M. van den Bosch, D. Klomp, Feasibility of 7 tesla breast magnetic resonance imaging determination of intrinsic sensitivity and high-resolution magnetic resonance imaging, diffusion-weighted imaging, and 1H-magnetic resonance spectroscopy of breast cancer patients receiving neoadjuvant therapy. Invest. Radiol. **46**, 370–376 (2011)
60. H. Rahbar, S. Partridge, W. DeMartini, B. Thursten, C. Lehman, Clinical and technical considerations for high quality breast MRI at 3 tesla. J. Magn. Reson. Imaging **37**, 778–790 (2013)
61. M.E. Ladd, High versus low state magnetic fields in MRI, in *Magnetic Resonance Imaging and Spectroscopy, Volume 3, Comprehensive Biomedical Physics*, ed. by Dž. Belkić, K. Belkić (Elsevier, Amsterdam, 2014), pp. 55–68
62. M. Tozaki, Proton MR spectroscopy of the breast. Breast Cancer **15**, 218–223 (2008)
63. M.E. Lippman, Breast cancer, in *Harrison's Principles of Internal Medicine*, 15th edn., ed. by E. Braunwald, A. Fauci, D.L. Kasper, S.L. Hauser, D.L. Longo, J.L. Jameson (McGraw-Hill, New York, NY, 2001), pp. 571–578
64. C.K. Kim, B.K. Park, Update of prostate magnetic resonance imaging at 3T. J. Comput. Assist. Tomogr. **32**, 163–172 (2008)
65. P. Bolan, L. DelaBarre, E. Baker, H. Merkle, L. Everson, D. Yee, M. Garwood, Eliminating spurious lipid sidebands in ^{1}H MRS of breast lesions. Magn. Reson. Med. **48**, 215–222 (2002)
66. P. Stanwell, C. Mountford, In vivo proton MR spectroscopy of the breast. Radiographics **27** (Suppl 1), S253–S266 (2007)
67. I.S. Gribbestad, B. Sitter, S. Lundgren, J. Krane, D. Axelson, Metabolite composition in breast tumors examined by proton nuclear magnetic resonance spectroscopy. Anticancer Res. **19**, 1737–1746 (1999)
68. R. Katz-Brull, D. Seger, D. Rivenson-Segal, E. Rushkin, H. Degani, Metabolic markers of breast cancer. Cancer Res. **62**, 1966–1970 (2002)
69. G. Eliyahu, T. Kreizman, H. Degani, Phosphocholine as a biomarker of breast cancer: molecular and biochemical studies. Int. J. Cancer **120**, 1721–1730 (2007)
70. K. Glunde, C. Jie, Z.M. Bhujwalla, Molecular causes of the aberrant choline phospholipid metabolism in breast cancer. Cancer Res. **64**, 4270–4276 (2004)
71. K. Glunde, J. Jiang, S.A. Moestue, I.S. Gribbestad, MRS/MRSI guidance in molecular medicine: targeting choline and glucose metabolism. NMR Biomed. **24**, 673–690 (2011)
72. Dž. Belkić, K. Belkić, *Signal Processing in Magnetic Resonance Spectroscopy with Biomedical Applications* (Taylor & Francis Group, London, 2010)

73. Dž. Belkić, *Quantum Mechanical Signal Processing and Spectral Analysis* (Taylor & Francis Group, London, 2005)
74. Dž. Belkić, Exact quantification of time signals in Padé-based magnetic resonance spectroscopy. Phys. Med. Biol. **51**, 2633–2670 (2006)
75. Dž. Belkić, Exponential convergence rate of the FPT for exact quantification in magnetic resonance spectroscopy. Phys. Med. Biol. **51**, 6483–6512 (2006)
76. Dž. Belkić, Machine accurate quantification in magnetic resonance spectroscopy. Nucl. Instrum. Methods Phys. Res **A 580**, 1034–1040 (2007)
77. Dž. Belkić, Strikingly stable convergence of the fast Padé transform (FPT) for high resolution parametric and non-parametric signal processing of Lorentzian and non-Lorentzian spectra. Nucl. Instrum. Methods Phys. Res. **A 525**, 366–371 (2004)
78. Dž. Belkić, K. Belkić, In vivo magnetic resonance spectroscopy by the fast Padé transform. Phys. Med. Biol. **51**, 1049–1075 (2006)
79. Dž. Belkić, The potential for practical improvements in cancer diagnostics by mathematically-optimized magnetic resonance spectroscopy. J. Math. Chem **49**, 2408–2440 (2011)
80. Dž Belkić, Exact signal–noise separation by Froissart doublets in the Fast Padé transform for MRS. Adv. Quantum Chem. **56**, 95–179 (2009)
81. A.C. Ojo, *The Analysis and Automatic Classification of Nuclear Magnetic Resonance Signals*. PhD Thesis, The University of Edinburgh (2010). Edinburgh Research Archive. http://hdl.handle.net/1842/4109
82. J.M. Zhang. *Human Brain Glutamate, Glutamine, γ-Aminobutyric Acid: Proton Magnetic Resonance Spectral Quantification with the Fast Padé Transform*. PhD Thesis. University of California Los Angeles (2013). http://escholarship.org/uc/item/1np12339
83. Dž. Belkić, K. Belkić, Exact quantification of time signals from magnetic resonance spectroscopy by the fast Padé transform with applications to breast cancer diagnostics. J. Math. Chem. **45**, 790–818 (2009)
84. L.F.A.G. Massuger, P.B.J. van Vierzen, U.F. Engelke, A. Heerschap, R.A. Wevers, 1H-magnetic resonance spectroscopy: a new technique to discriminate benign from malignant ovarian tumors. Cancer **82**, 1726–1730 (1998)
85. A. Esseridou, G. Di Leo, L.M. Sconfienza, V. Caldiera, F. Raspagliesi, B. Grijuela, F. Hanozet, F. Podo, F. Sardanelli, In vivo detection of choline in ovarian tumors using 3D MRS. Invest. Radiol. **46**, 377–382 (2011)
86. E.A. Boss, S.H. Moolenaar, L.F.A.G. Massuger, H. Boonstra, U.F.H. Engelke, J.G.N. de Jong, R.A. Wevers, High-resolution proton nuclear magnetic resonance spectroscopy of ovarian cyst fluid. NMR Biomed. **13**, 297–305 (2000)
87. K. Belkić, Resolution performance of the fast Padé transform: potential advantages for magnetic resonance spectroscopy in ovarian cancer diagnostics. Nucl. Instrum. Methods Phys. Res. A **580**, 874–880 (2007)
88. Dž. Belkić, K. Belkić, Mathematical modeling applied to an NMR problem in ovarian cancer detection. J. Math. Chem. **43**, 395–425 (2008)
89. C.H. Bangma, M. Bul, M. Roobol, The Prostate Cancer Research International: active surveillance study. Curr. Opin. Urol. **22**, 216–221 (2012)
90. M. Center, A. Jemal, J. Lortet-Tieulent, E. Ward, J. Ferlay, O. Brawley, F. Bray, International variation in prostate cancer incidence and mortality rates. Eur. Urol. **61**, 1079–1092 (2012)
91. T. Scheenen, J. Fütterer, E. Weiland, P. van Hecke, M. Lemort, C. Zechmann, H.-P. Schlemmer, D. Broome, G. Villeirs, J. Lu, J. Jelle Barentsz, S. Roell, A. Heerschap, Discriminating cancer from noncancer tissue in the prostate by 3-dimensional proton magnetic resonance spectroscopic imaging: a prospective multicenter validation study. Invest. Radiol. **46**, 25–33 (2011)
92. A. Shukla-Dave, H. Hricak, C. Moskowitz, N. Ishill, O. Akin, K. Kuroiwa, J. Spector, M. Kumar, V. Reuter, J. Koutcher, K. Zakian, Detection of prostate cancer with MR spectroscopic imaging: an expanded paradigm incorporating polyamines. Radiology **245**, 499–506 (2007)
93. C. Testa, R. Schiavina, R. Lodi, E. Salizzoni, C. Tonon, A. D'Errico, B. Corti, A. Morselli-Labate, A. Franceschelli, A. Bertaccini, F. Manferrarik, W. Grigioni, R. Canini, G. Martorana, B. Barbiroli, Accuracy of MRI/MRSI-based transrectal ultrasound biopsy in peripheral and transition zones of the prostate gland in patients with prior negative biopsy. NMR Biomed. **23**, 1017–1026 (2010)

94. A.C. Westphalen, D. McKenna, J. Kurhanewicz, F. Coakley, Role of magnetic resonance imaging and magnetic resonance spectroscopic imaging before and after radiotherapy for prostate cancer. J. Endourol. **22**, 789–794 (2008)
95. M. Swanson, A. Zektzer, Z. Tabatabai, J. Simko, S. Jarso, K. Keshari, L. Schmitt, P. Carroll, K. Shinohara, D. Vigneron, J. Kurhanewicz, Quantitative analysis of prostate metabolites using 1H HRMAS spectroscopy. Magn. Reson. Med. **55**, 1257–1264 (2006)
96. Dž. Belkić, K. Belkić, Unequivocal resolution of multiplets in MRS for prostate cancer by the FPT. J. Math. Chem. **45**, 819–858 (2009)
97. Dž. Belkić, K. Belkić, Molecular imaging and magnetic resonance for improved target definition in radiation oncology, in *Radiation Damage to Biomolecular Systems*, ed. by G. Gómez, M.C. Fuss (Springer, Berlin, 2012), pp. 411–429
98. Dž. Belkić, K. Belkić, Magnetic resonance spectroscopy with high-resolution and exact quantification in the presence of noise for improving ovarian cancer detection. J. Math. Chem. **50**, 2558–2576 (2012)
99. Dž. Belkić, K. Belkić, Resolution enhancement as a key step towards clinical implementation of Padé-optimized magnetic resonance spectroscopy for diagnostic oncology. J. Math. Chem **51**, 2608–2637 (2013)
100. J. Wijnen, W. van der Kemp, M. Luttje, M. Korteweg, P. Luijten, D. Klomp, Quantitative 31P magnetic resonance spectroscopy of the human breast at 7T. Magn. Reson. Med. **68**, 339–348 (2012)
101. Dž. Belkić, K. Belkić, The role of optimized molecular imaging in personalized cancer medicine. Diagn. Imag. Eur. **30**(4), 28–31 (2014)
102. S. Meisamy, P. Bolan, E. Baker, R. Bliss, E. Gulbahce, L. Everson, M. Nelson, T. Emory, T. Tuttle, D. Yee, M. Garwood, Neoadjuvant chemotherapy of locally advanced breast cancer: predicting response with in vivo 1H MR spectroscopy—a pilot study at 4T. Radiology **233**, 424–431 (2004)
103. H. Shin, H.-M. Baek, J.-H. Ahn, S. Baek, H. Kim, J. Cha, H. Kim, Prediction of pathologic response to neoadjuvant chemotherapy with breast cancer using diffusion-weighted imaging and MRS. NMR Biomed. **25**, 1349–1359 (2012)
104. M. Tozaki, M. Sakamoto, Y. Oyama, K. Maruyama, E. Fukuma, Predicting pathological response to neoadjuvant chemotherapy in breast cancer with quantitative 1H MR spectroscopy using the external standard method. J. Magn. Reson. Imaging **31**, 895–902 (2010)
105. L. Jiang, T. Greenword, D. Artemov, V. Raman, P. Winnard, R. Heeren, Z. Bhujwalla, K. Glunde, Localized hypoxia results in spatially heterogeneous metabolic signatures in breast tumor models. Neoplasia **14**, 732–741 (2012)
106. Dž. Belkić, K. Belkić, Mechanistic repair-based Padé linear-quadratic model for cell response to radiation damage. Adv. Quantum Chem. **65**, 407–449 (2013)
107. Dž. Belkić, K. Belkić, Mechanistic description of survival of irradiated cells: repair kinetics in Padé linear-quadratic or differential Michaelis–Menten model. J. Math. Chem. **51**, 2572–2607 (2013)
108. Dž. Belkić, Survival of radiation-damaged cells via mechanism of repair by pool molecules: the Lambert function as the exact analytical solution of coupled kinetic equations. J. Math. Chem **52**, 1201–1252 (2014)
109. Dž. Belkić, Repair of irradiated cells by Michaelis–Menten enzyme catalysis: the Lambert function for integrated rate equations in description of surviving fractions. J. Math. Chem. **52**, 1253–1291 (2014)